

REPORT DOCUMENTATION PAGE			Form Approved OMB NO. 0704-0188		
<p>The public reporting burden for this collection of information is estimated to average 1 hour per response, including the time for reviewing instructions, searching existing data sources, gathering and maintaining the data needed, and completing and reviewing the collection of information. Send comments regarding this burden estimate or any other aspect of this collection of information, including suggestions for reducing this burden, to Washington Headquarters Services, Directorate for Information Operations and Reports, 1215 Jefferson Davis Highway, Suite 1204, Arlington VA, 22202-4302. Respondents should be aware that notwithstanding any other provision of law, no person shall be subject to any penalty for failing to comply with a collection of information if it does not display a currently valid OMB control number.</p> <p>PLEASE DO NOT RETURN YOUR FORM TO THE ABOVE ADDRESS.</p>					
1. REPORT DATE (DD-MM-YYYY) 28-08-2015		2. REPORT TYPE Ph.D. Dissertation		3. DATES COVERED (From - To) -	
4. TITLE AND SUBTITLE Statistical Moments in Variable-Density Incompressible Rayleigh-Taylor Flows			5a. CONTRACT NUMBER W911NF-13-1-0249		
			5b. GRANT NUMBER		
			5c. PROGRAM ELEMENT NUMBER 611102		
6. AUTHORS Wenlin_Hu_			5d. PROJECT NUMBER		
			5e. TASK NUMBER		
			5f. WORK UNIT NUMBER		
7. PERFORMING ORGANIZATION NAMES AND ADDRESSES Research Foundation of SUNY at Stony Br W-5510 Melville Library Stony Brook, NY 11794 -3362			8. PERFORMING ORGANIZATION REPORT NUMBER		
9. SPONSORING/MONITORING AGENCY NAME(S) AND ADDRESS (ES) U.S. Army Research Office P.O. Box 12211 Research Triangle Park, NC 27709-2211			10. SPONSOR/MONITOR'S ACRONYM(S) ARO		
			11. SPONSOR/MONITOR'S REPORT NUMBER(S) 63848-MA.26		
12. DISTRIBUTION AVAILABILITY STATEMENT Approved for public release; distribution is unlimited.					
13. SUPPLEMENTARY NOTES The views, opinions and/or findings contained in this report are those of the author(s) and should not be construed as an official Department of the Army position, policy or decision, unless so designated by other documentation.					
14. ABSTRACT Mix is critical to the modeling of chemical or nuclear reaction processes in fluids. We simulate Rayleigh-Taylor unstable pre-turbulent and transitionally turbulent fluid mixing regimes. We model experiments generated by the flow of hot and cold water over a splitter plate into an observation channel. Three statistical second moments of the flow were measured. Our simulations achieve excellent agreement with two of these and partial agreement with the third. We draw two broader lessons from this study. The first is that numerical algorithms do matter. We compare our					
15. SUBJECT TERMS Fluid Mixing, Rayleigh-Taylor Mixing, Turbulent Kinetic Energy, Statistical Moments of Turbulent Flow					
16. SECURITY CLASSIFICATION OF:			17. LIMITATION OF ABSTRACT	15. NUMBER OF PAGES	19a. NAME OF RESPONSIBLE PERSON
a. REPORT UU	b. ABSTRACT UU	c. THIS PAGE UU			James Glimm
					19b. TELEPHONE NUMBER 631-632-8370

Report Title

Statistical Moments in Variable-Density Incompressible Rayleigh-Taylor Flows

ABSTRACT

Mix is critical to the modeling of chemical or nuclear reaction processes in fluids. We simulate Rayleigh-Taylor unstable pre-turbulent and transitionally turbulent fluid mixing regimes. We model experiments generated by the flow of hot and cold water over a splitter plate into an observation channel. Three statistical second moments of the flow were measured. Our simulations achieve excellent agreement with two of these and partial agreement with the third.

We draw two broader lessons from this study. The first is that numerical algorithms do matter. We compare our simulations to one obtained using Miranda, a 10th-order compact stencil turbulent code. However, this code lacks front tracking, an important aspect of our simulation algorithm. The Miranda simulation misses data error bars for the measure of mix over most of the experimental time, although it is nearly DNS and uses mesh two, four and eight times finer than what we report here.

The second broader lesson is that details of data analysis matter. The velocity statistics are generated by two laser sheets in rapid succession, to track particles seeded into the flow and to generate the resulting velocity statistics. This methodology suppresses particles and fluid elements with motion normal to the laser sheet, a result that biases the second moments as reported. Consequently, the experimentally reported second moments are not suitable for direct use in the calibration of RANS simulation codes. Rather, as reported here, LES simulations, validated against the biased statistics, can be used to construct unbiased statistics, and these are suitable for setting RANS parameters.

Statistical Moments in Variable-Density Incompressible Mixing Flows

A Dissertation Presented

by

Wenlin Hu

to

The Graduate School

in Partial Fulfillment of the

Requirements

for the Degree of

Doctor of Philosophy

in

Applied Mathematics and Statistics

Stony Brook University

August 2015

Stony Brook University

The Graduate School

Wenlin Hu

We, the dissertation committee for the above candidate for the
Doctor of Philosophy degree, hereby recommend
acceptance of this dissertation.

James Glimm - Dissertation Advisor

Professor, Dept. of Applied Mathematics and Statistics

Xiangmin Jiao - Chairperson of Defense

Associate Professor, Dept. of Applied Mathematics and Statistics

Roman Samulyak - Committee Member

Professor, Dept. of Applied Mathematics and Statistics

Michael Zingale - Outside Member

Associate Professor, Dept. of Physics and Astronomy

This dissertation is accepted by the Graduate School

Charles Taber

Dean of the Graduate School

Abstract of the Dissertation

Statistical Moments in Variable-Density Incompressible Mixing Flows

by

Wenlin Hu

Doctor of Philosophy

in

Applied Mathematics and Statistics

Stony Brook University

2015

Mix is critical to the modeling of chemical or nuclear reaction processes in fluids. We simulate Rayleigh-Taylor unstable pre-turbulent and transitionally turbulent fluid mixing regimes. We model experiments generated by the flow of hot and cold water over a splitter plate into an observation channel. Three statistical second moments of the flow were measured. Our simulations achieve excellent agreement with two of these and partial agreement with the third.

We draw two broader lessons from this study. The first is that numerical algorithms do matter. We compare our simulations to one obtained using Miranda, a 10^{th} -order compact stencil turbulence code. However, this code lacks front tracking, an important aspect of our simulation algorithm. The Miranda simulation misses data error bars for the measure of mix over most of the experimental time, although it is nearly DNS and uses mesh two, four and eight times finer than what we report here.

The second broader lesson is that details of data analysis matter. The velocity

statistics are generated by two laser sheets in rapid succession, to track particles seeded into the flow and to generate the resulting velocity statistics. This methodology suppresses particles and fluid elements with motion normal to the laser sheet, a result that biases the second moments as reported. Consequently, the experimentally reported second moments are not suitable for direct use in the calibration of RANS simulation codes. Rather, as reported here, LES simulations, validated against the biased statistics, can be used to construct unbiased statistics, and these are suitable for setting RANS parameters.

To my grandparents, parents and beloved wife

Table of Contents

List of Figures	viii
List of Tables	xii
Acknowledgments	xiii
1 Introduction	1
1.1 Overview and Motivation	1
1.2 Rayleigh-Taylor Instability	6
1.3 Dissertation Organization	9
2 Mathematical Model and Numerical Methods	11
2.1 Incompressible Tracking	11
2.1.1 Governing Equations	12
2.1.2 Numerical Algorithms	13

2.1.3	Front Tracking and Ghost Cell Method	22
2.1.4	Simulation Parameters, Initial and Boundary Conditions	27
2.2	A New FronTier Package	35
3	Results and Discussion	36
3.1	Evolution of the Rayleigh-Taylor Mixing Zone	37
3.2	Mixing Zone Growth	39
3.3	Molecular Mixing Parameter	42
3.4	Velocity Variances	42
3.4.1	Particle-Image Velocimetry Diagnostics in Experiment	45
3.4.2	PIV Diagnostics VS FronTier Diagnostics	46
3.5	Justification of the Omission of SGS Terms	51
3.6	Discussion	51
4	Conclusions	56
	Bibliography	58

List of Figures

1.1	Schematic diagram of the water channel and its associated diagnostics. Camera: 640H×480V pixels, 1200 image capacity on board. Lasers: two 120 mJ Nd-YAG, 15 Hz pulse, sample rate 30 s ⁻¹ , thickness 532 nm. Thermocouple: E-type, 0.16 mm diameter, 100 kHz, sampling at 12 bit accuracy. The dimensions of the mixing section of the channel are 100 cm × 20 cm × 32 cm, in x -, y -, and z -directions, respectively.	3
2.1	Plot of three grids with positioning of variables for 2-D. We denote the cell center as (i, j) , the cell faces as $(i + 1/2, j)$ and $(i, j + 1/2)$, and the cell vertices as $(i \pm 1/2, j \pm 1/2)$ and $(i \pm 1/2, j \mp 1/2)$. The MAC grid is used in the FronTier simulations.	15
2.2	Plot of standard and expanded stencils for the two-dimensional Lapla- cian. The standard stencil consists of the grid (i, j) and 4 neighboring grids marked with "×", while the expanded stencil uses neighboring grids marked with "○".	16
2.3	Plot of the basic geometrical data structures employed by the front track- ing method for three dimensions.	23

2.4	Flowchart for the front tracking framework. To follow the best practices, the interface/front library is developed/debugged/tested/maintained independently from a variety of physics application libraries in FronTier.	24
2.5	Plot of a two-dimensional irregular cell (i, j) , with the black component. The cell is irregular w.r.t. its west and north neighbors, however, it is regular w.r.t. its east and south neighbors. The ghost density ρ_{ij} is used as the real density on the west and north (ghost) cells, but the east and south (normal) cells use their original densities $\rho_{i+1,j}$ and $\rho_{i,j-1}$.	26
2.6	Plot of the initial density field on the FronTier medium grid. The width of the initial diffusion layer $\varepsilon = 0.174$ cm, so that three FronTier simulations can meet the first available experimental data point for the molecular mixing parameter θ . For better visual effect, a partial computational domain is presented here.	31
2.7	Plot of the initial two-dimensional interfacial perturbation $\zeta(x, y)$ on the FronTier medium grid. $\zeta(x, y)$ is modeled using the interfacial perturbation spectra from the hot/cold water channel experiment in the x - and y -directions.	32
2.8	Plots of the initial velocity field on the FronTier medium grid, where u , v , and w are streamwise, spanwise, and vertical velocities, respectively. The v velocity is negligible everywhere. Both u and w velocities take their maximum values at the midplane and exponentially decay with vertical distance from the midplane.	34

3.1	Photograph of the early-time development of the mixing zone in the water channel experiment. The mean flow is from left to right, corresponding to a dimensionless time interval $\tau \in [0, 0.8]$	38
3.2	Plots of the tracked interfaces for the FronTier medium grid simulation VS the $f_1 = 0.5$ volume fraction isosurfaces for the Miranda simulation, at selected τ 's. Here, x -, y -, and z -directions are streamwise, spanwise, and vertical directions, respectively.	41
3.3	Plot of mixing zone growth for three FronTier simulations, one Miranda simulation and experimental data. The slower simulation growth at earlier times is likely due to incorrect modeling of the initial perturbations.	43
3.4	Plot of $\theta(\tau) = \langle f(1 - f) \rangle / (\langle f \rangle \langle 1 - f \rangle)$ on the center plane of the mixing zone as a function of the dimensionless time τ , for three FronTier simulations, one Miranda simulation and experimental data.	44
3.5	Schematic diagram of the region measured by the PIV diagnostics system in the water channel.	45
3.6	Schematic diagram of a basic model for estimating the escape velocity v_{esc} . It shows the entering and leaving positions of the particle with a mean particle diameter $D_p = 13 \mu\text{m}$. The laser sheet is parallel to the xz -plane, with a thickness of $L = 0.532 \mu\text{m}$	48
3.7	Plots of normalized vertical velocity variance $\langle w'^2 \rangle / AgH$ and streamwise velocity variance $\langle u'^2 \rangle / AgH$ for three FronTier simulations with the velocity filter and one Miranda simulation, with experimental data superimposed.	49

3.8	Plots of normalized vertical velocity variance $\langle w'^2 \rangle / AgH$ and streamwise velocity variance $\langle u'^2 \rangle / AgH$ for FronTier simulation on the medium grid with and without the velocity filter.	50
3.9	Plot of the ratios of the mean turbulent kinematic viscosity $\langle \nu_{\text{turb}} \rangle$ and diffusivity $\langle D_{\text{turb}} \rangle$ in the RT mixing zone to the molecular kinematic viscosity $\nu = (\mu_1 + \mu_2) / (\rho_1 + \rho_2)$ and diffusivity $D = \nu / \text{Sc}$. The SGS terms are small relative to the molecular viscosity/diffusion, even for the FronTier coarse grid.	52
3.10	Plots of the mixing zone growth, molecular mixing parameter, and velocity variances for the FronTier coarse grid simulation with/without the SGS terms. In each plot, two curves are almost overlapped, even at late times.	53

List of Tables

2.1	Table of simulation parameters used in the FronTier simulations	28
2.2	Table of wave numbers $\mathbf{k} = (k_x, k_y)$ and mode amplitudes $A(\mathbf{k})$ and \hat{w} in FronTier simulations	30
3.1	Table of selected percentage of outliers on FronTier fine grid	48

Acknowledgments

I would like to express my profound gratitude to my advisor, Professor James Glimm, for suggesting this important and exciting thesis topic and for his advice, support, encouragement and guidance toward my Ph.D. degree. He taught me not only the way to do scientific research, but also the way to become a professional scientist. He was always enthusiastic about my education. He is my advisor and a lifetime role model for me.

I would like to thank Professor Xiangmin Jiao. He provided encouragement and valuable technical knowledge, especially the high-order differential geometry operations and its implementation. It is a great honor to have Professor Roman Samulyak and Professor Michael Zingale to be my dissertation committee members. I really appreciate all the valuable suggestions they made to improve and perfect this dissertation.

I would like to thank all my friends during my years of study as a graduate student at Stony Brook for their friendship and encouragement. Special thanks goes to Dr. Hyunkyung Lim for so many inspiring discussion we have had together.

Sincere thanks to my family, especially my wife Jingwen. It is your endless support and love that make me strong enough to face all the challenges during my pursue of

the Ph.D. degree. I should never been able to overcome the endless difficulties in both studying and living without your encouragement.

Chapter 1

Introduction

1.1 Overview and Motivation

Mix (either molecular level mixing, or fine scale granularity of flow mixtures) occurs in both turbulent and nonturbulent flows. Mix is an significant aspect of many flows, with important roles in combustion, chemical processing and food preparation, among other applications [70]. Mix of reactive components can enhance reactions, while admixture of non-reactive constituents can retard it. Thus, we see the importance of turbulent mix to theories of turbulent combustion and turbulent nuclear reactive processes. The flows we analyze have a maximum $Re = 600K$, and span a range from laminar to pre-turbulent or incipient turbulent flows.

In previous work, see [56, 57] and references cited there, we achieved systematic agreement between simulation and experiment for the growth rate α of a Rayleigh-Taylor unstable mixing zone. Continuing this line of research [43], we analyzed the influence of the long wave modes in the initial data and found an influence on α

of about 5%, thereby questioning the common claim that long wave length noise in the initial data accounts for commonly observed discrepancies between simulation and experiment. The experiment so modeled used immiscible fluids, so that the boundary of the early time bubbles was clearly visible. We note that surface layer effects do not invalidate the conclusions of this study. Specifically such effects can be of two types. They can enhance the instabilities at the boundary or suppress them. In the latter case, the face-on view will see bulk not boundary effects and the analysis is correct as claimed. In the latter case, with the bulk effects possibly smaller than the observed boundary effects, and the boundary effects giving only a 5% effect upon α , the bulk early time perturbations will be smaller, so that the reported result remains valid as an upper bound.

In [52], we established convergence of statistical moments, probability density functions (PDFs) and cumulative distribution functions (CDFs) under mesh refinement, using a novel, stochastically motivated, notion of convergence. We have argued on several occasions, see for example [41, 40], that the solutions of turbulent mixing problems are nonunique at a numerical level. The nonuniqueness arises from, and is ameliorated by, the use of dynamic subgrid scale terms; in addition, it arises from numerical truncation error, serving as a proxy for subgrid scale turbulent transport. For this reason, experimental validation in simulations of mixing is of great importance.

Here we are concerned with validation of simulations. The experiments [68] are generated by the flow of hot (light) and cold (heavy) water over a 3.2 mm thick splitter plate and into a viewing channel horizontally, see Fig. 1.1. In the channel, buoyancy forces give rise to a Rayleigh-Taylor mixing process as the hot (light, below) fluid rises through the cold (heavy, above) fluid, where the density difference is induced by the temperature difference $T_{\text{diff}} \approx 5^\circ\text{C}$.

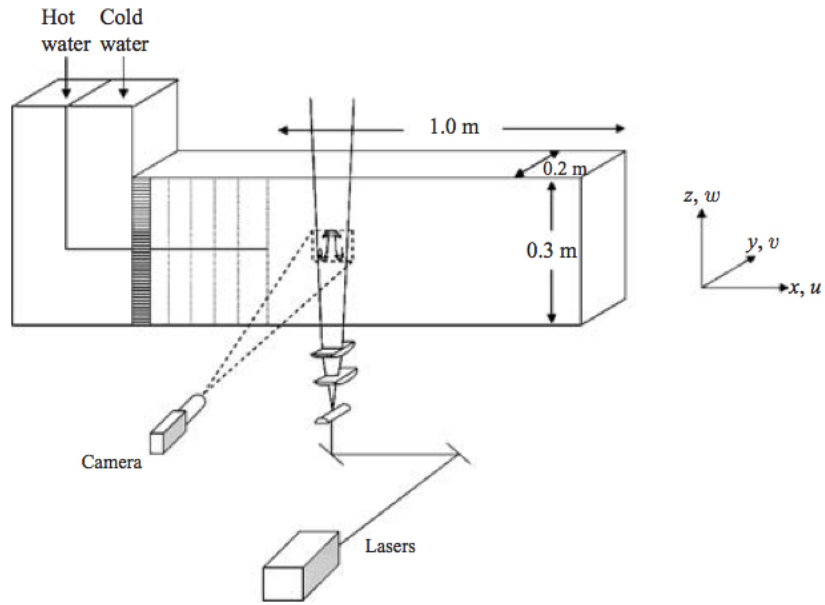


Figure 1.1: Schematic diagram of the water channel and its associated diagnostics. Camera: $640H \times 480V$ pixels, 1200 image capacity on board. Lasers: two 120 mJ Nd-YAG, 15 Hz pulse, sample rate 30 s^{-1} , thickness 532 nm. Thermocouple: E-type, 0.16 mm diameter, 100 kHz, sampling at 12 bit accuracy. The dimensions of the mixing section of the channel are $100 \text{ cm} \times 20 \text{ cm} \times 32 \text{ cm}$, in x -, y -, and z -directions, respectively.

We study second moments of the temperature and velocity statistics and related quantities. Of the three statistical quantities recorded, we obtain excellent agreement with two and partial agreement with a third.

From this study, we emphasize two broader points.

First, the numerical algorithm used does matter. The choice of numerical algorithm for the modeling of mix is important. The very strong validation record of the authors and co-workers, and the results reported here are with the use of front tracking. Front tracking is a Lagrangian addition to an otherwise Eulerian simulation. Due to the complex nature of the mixing flows, Eulerian methods are needed to avoid mesh tangling and distortion. But Lagrangian methods are needed to avoid numerical diffusion. The compromise is Arbitrary Lagrangian Eulerian (ALE) algorithms [11, 12, 13, 26, 49, 64], which allow Lagrangian methods for a longer portion of the instability development than a pure Lagrangian simulation would. These eventually also become pure Eulerian, and lose their advantage at late time. Front tracking can be thought of as ALE algorithm, in that the Lagrangian aspect of the computation is confined to a surface. As a result, and due to development of the front tracking algorithm, this method is able to retain its important Lagrangian aspect far later than would be possible with conventional ALE algorithms. In the present simulations, we continue the tracking until the end of the experimentally observed times, so that the Lagrangian aspect is never removed.

In view of our claim that this methodology is important for a wide class of mixing problems, we have developed an Application Programming Interface (API), to allow easier insertion of this algorithm into other physics codes [53]. In addition to organizing our own code as a pure hydro code with the tracking accessed through the API, we have (with co-workers) used the API to add tracking to the High Energy Density Physics

(HEDP) code FLASH [34] from the University of Chicago.

Our second main point is that details of the data analysis do matter. It is commonly the case that the directly measured quantities are convolved in some manner with the measurement process, and it is not always possible to deconvolve the measurement from the directly measured data. In these cases, it is more straightforward to emulate the measurement instrument within the simulation, and obtain synthetic measurements, to be compared with the experiment. The simulation, once validated in this manner, will produce directly important flow details, with a high level of confidence. In many fluid mixing experiments, velocity statistics are gathered from a pair of laser sheet images, captured in rapid succession, known as Particle Image Velocimetry (PIV) [2, 3]. Seed particles in the flow, when they show up in both images with a small displacement, offer a local velocity measurement. This method, used in the present experiments, suppresses velocities nearly normal to the laser sheet, as the associated seed particles show up in only one of the pair of laser images. Suppression of such velocities, noted by experimentalists, is shown here to be serious, in the sense that the recorded second moments are significantly biased by it. It follows that the experimentally recorded velocity second moments cannot be used directly for scientific purposes, such as the setting of unknown parameters in a RANS model. Rather they can only be used as validation for a direct LES or DNS model of the experiment itself. Once so modeled, the full second moments of the velocities from the simulation acquire a scientific meaning and confidence, which allows their use, for example in the setting of RANS parameters. Alternatively, the issue is addressed at an experimental level, with the use of wider laser sheets. In summarizing this discussion, we would say that the LES or DNS simulation can be an essential part of an experiment, when it accomplishes the deconvolution of the instrument from the observations, to yield directly

desired data.

1.2 Rayleigh-Taylor Instability

Rayleigh-Taylor instability (RTI) occurs whenever light fluid pushes into a heavy fluid [62, 83, 19, 20, 30, 79]. The ensuing turbulent transport and mixing has far-reaching consequences in a variety of contexts, such as supernovae [54, 35, 91], geophysics [45, 86], combustion [18, 84], inertial confinement fusion (ICF) capsules [33, 72, 60], and etc. RTI flows are adopted as an important verification and validation (V&V) test case for hydrodynamic codes.

Youngs [87] described the development of a RT mixing zone as a three-stage process: Initially an exponential and independent growth of infinitesimal perturbations for each mode, according to linear stability analysis [19, 27]. As the amplitude of a particular mode approaches half of its wave length, the instability saturates and longer wave lengths (that have yet to reach saturation) take over. Emmons et al. [31] proposed the term "bubble competition" to describe this regime. Eventually, through nonlinear mode interaction and successive wave length saturation, a self-similar RT mixing zone is formed with a scale similarity believed to be gt^2 [32, 79, 87, 42]. The past decades have seen these stages being refined and challenged, which are still an open issue.

In the linear stage, the exponential growth rate s of a single mode is captured by the linear stability theory (LST). Under certain idealized conditions, e.g. in the absence of surface tension and viscosity, it holds that $s = \sqrt{k g A}$, where $k = 2\pi/\lambda$ is the wave number, λ is the plane wave length, g is the gravity acceleration, and $A := (\rho_H - \rho_L)/(\rho_H + \rho_L)$ is the Atwood number [19], with ρ_L and ρ_H representing

the densities of the light and heavy fluids, respectively. The Atwood number A is the primary dimensionless parameter characterizing the gravity acceleration effects. If stabilizing effects of only surface tension γ are imposed [20], the growth rate changes to

$$s_\gamma = \sqrt{kgA - \frac{k^3\gamma}{\rho_H + \rho_L}} \quad (1.1)$$

with a "cut-off" wave length $\lambda_{\gamma,c}$ (i.e. all wave lengths above are unstable, and those below, as s_γ becomes imaginary, are stable) given by

$$\lambda_{\gamma,c} = \frac{2\pi}{k_{\gamma,c}} = 2\pi\sqrt{\frac{\gamma}{g(\rho_H - \rho_L)}} \quad (1.2)$$

The "most unstable" wave length λ_m that grows fastest is

$$\lambda_{\gamma,m} = \lambda_{\gamma,c}\sqrt{3} \quad (1.3)$$

Duff et al. [30] derived the growth rate from a linear stability analysis when viscous/diffusive effects considered.

With regard to the nonlinear stage of single-mode RT instability, many approaches have been proposed for modeling the late-time steady bubble velocity [55, 79, 5, 88, 44, 1, 75]. For example, the model by Goncharov [44] predicts the saturation velocity of a two-dimensional bubble with wave number k ,

$$V_{b,\infty}^{2D} = 1.025\sqrt{\frac{2A}{1+A}\frac{g}{3k}} \quad (1.4)$$

and for a three dimensional bubble

$$V_{b,\infty}^{3D} = 1.02\sqrt{\frac{2A}{1+A}\frac{g}{k}} \quad (1.5)$$

At high Atwood number $A \approx 1$, these formulas reduce to those of Layzer [55].

At late times, the self-similarity width of the multi-mode RT unstable mixing region is described by

$$h(t) := h_b(t) + h_s(t) \approx \alpha A g t^2 \quad (1.6)$$

where h_b and h_t represent bubble and spike front widths. This formula defines α , a dimensionless growth rate parameter, that has been the center of RT research over the past decades.

Another important dimensionless parameter of the multi-mode RT instability is the molecular mixing parameter θ , which is a common measure of mixing and defined as the normalized second moment or normalized correlation function

$$\theta = \frac{\langle f(1-f) \rangle}{\langle f \rangle \langle 1-f \rangle} \quad (1.7)$$

where $f = (\rho - \rho_i)/(\rho_j - \rho_i)$ is the heavy/light fluid volume fraction (between 0 and 1 inclusively). If there is no mixing, f takes on values 0 or 1 and $\theta = 0$, while if there is perfect mixing $f = 1 - f = 1/2$ and $\theta = 1$. In simple models of second order chemistry, the reaction rate is proportional to θ times the Arrhenius factor.

Since 1950's, A wide variety of experiments have been performed to study the small Atwood number Rayleigh-Taylor instabilities in fluids. While an overview of the RT experiments is beyond the scope of the present study, we mention two typical experiments, against which the previous FronTier simulations have been successfully validated [56, 57, 43]. A review on the small Atwood number RT experiments is given in [6].

1. The "rocket rig" experiments [77, 17, 80], which include significant measurements

of the growth of a multi-mode Rayleigh-Taylor mixing layer using a drop tank. The tank is filled with light fluid over heavy fluid and accelerated downward by rocket motors. These experiments have no measurement of the initial conditions or of the internal structure of the mixing layer.

2. The water channel experiments [74, 68], which have been incorporated with a set of diagnostics devices to facilitate measuring of the parameterized initial temperature/velocity/interfacial perturbations, as described in the previous section 1.1.

1.3 Dissertation Organization

Chapter 1 gives a brief overview of very strong validation record with the use of front tracking for a series of turbulent mixing problems. Then it shows the motivation of studying the statistical second moments of the mixing flow. A concise overview of the Rayleigh-Taylor instability is given as well.

Chapter 2 presents the governing equations for the variable-density incompressible RT flow. Followed is an incompressible tracking algorithm that couples a second-order MAC projection and front tracking method. Then it summarizes the simulation parameters, initial and boundary conditions. A new FronTier package is introduced in the end.

Chapter 3 displays plots of the RT unstable mixing zone evolution, the mixing layer growth, and three statistical second moments of the flow, comparing three FronTier simulations to the Miranda simulation and experimental data. The results show significant improvement relative to the results of the Miranda simulation, and exhibit

strong experimental validation for most statistical moments. Followed is the justification of the omission of SGS terms for FronTier simulations. The section ends with a discussion of our statistical results.

Chapter 4 concludes the study with two points. First, the choice of numerical algorithms is significant in simulations of statistical second moments, and front tracking is an important aspect of a good algorithm to choose for turbulent mixing. Secondly, details of data analysis matter. We attribute an initially observed simulation-experiment discrepancy to insufficient modeling of the data collection.

Chapter 2

Mathematical Model and Numerical Methods

2.1 Incompressible Tracking

The incompressible version of the front tracking code has been described previously [90, 59]. The algorithm uses an approximate projection method [16] with the interface modeled with the Immersed Boundary Method (IBM), as spread via a numerical approximation to the Heaviside function over a few mesh blocks [71, 66]. For the present work, we upgrade the algorithm to support variable-density incompressible Rayleigh-Taylor flow. A second-order MAC projection method is employed to solve the variable-density incompressible flow.

2.1.1 Governing Equations

The variable-density incompressible continuity, momentum equations, and concentration equations are [24]

$$\frac{\partial \rho}{\partial t} + \nabla \cdot (\rho U) = 0 \quad (2.1)$$

$$\rho \left(\frac{\partial U}{\partial t} + (U \cdot \nabla) U \right) = \rho \vec{g} - \nabla p + \nabla \cdot \tau \quad (2.2)$$

$$\frac{\partial(\rho c_l)}{\partial t} + \nabla \cdot (\rho c_l U) = \nabla \cdot (\rho D \nabla c_l) \quad (2.3)$$

where ρ is the total density, $U = (u, v, w)$ is the velocity vector field, $\vec{g} = (0, 0, -g)$ is the gravity vector field, p is the pressure, $\tau_{ij} = \mu (\partial u_i / \partial x_j + \partial u_j / \partial x_i - (2/3) \delta_{ij} (\nabla \cdot U))$ is the viscous stress tensor with kinematic viscosity $\nu = (\mu_1 + \mu_2) / (\rho_1 + \rho_2)$ and dynamic viscosity $\mu = \rho \nu$, c_l is the concentration of fluid l ($l = 1, 2$), and D is the binary diffusivity. As per [67], the temperature equation is not solved; instead, one of the concentration equations is solved.

The concentration is related to the total density. For example, c_1 is defined as

$$\frac{1}{\rho} = \frac{c_1}{\rho_1} + \frac{1 - c_1}{\rho_2} \quad (2.4)$$

Equations (2.1), (2.3), and (2.4) together imply a non-solenoidal vector field [51].

The derivation of the divergence constraint is as follows. Eq. (2.4) gives

$$c_1 = \frac{(\rho_2 - \rho) \rho_1}{(\rho_2 - \rho_1) \rho} \quad (2.5)$$

Substituting c_1 into Eq. (2.3) where $l = 1$ yields:

$$-\frac{\partial \rho}{\partial t} + \nabla \cdot (\rho_2 U) - \nabla \cdot (\rho U) = \nabla \cdot (\rho \rho_2 D \nabla (\frac{1}{\rho})) \quad (2.6)$$

Substitute Eq. (2.1) into Eq. (2.6) and simplify the equation, we obtain the divergence constraint

$$\nabla \cdot U = -\nabla \cdot (\frac{D}{\rho} \nabla \rho) := S \quad (2.7)$$

Our simulations are LES. Due to the strong mixing and transitional/marginal turbulent nature of the flow, the dynamic subgrid-scale (SGS) terms [38, 63, 58] are computed to have small coefficients and were accordingly omitted, thus our simulations are Implicit LES (ILES). The justification of the omission of the SGS terms is presented in Sec. 3.5.

2.1.2 Numerical Algorithms

The original projection method for computing incompressible Navier-Stokes equations was introduced by Chorin [21, 22]. It predicts an intermediate vector field which is then projected onto the space of divergence-free vectors. Based on the idea of a Hodge decomposition $V = V^d + \nabla \phi$, the method uses the discrete divergence and gradient operators, \mathcal{D} and \mathbf{G} , which are required to be skew adjoint, $\mathcal{D} = -\mathbf{G}^T$, or as an inner product,

$$(\mathcal{D}V, \phi)_s = -(V, \mathbf{G}\phi)_v \quad (2.8)$$

where $(\cdot, \cdot)_s$ and $(\cdot, \cdot)_v$ represent a pair of inner products on discrete scalar and vector fields, respectively. Eq. (2.8) guarantees that the discrete projection is orthogonal, and as a result the discrete divergence is exactly zero. Taking the divergence of the Hodge

decomposition gives $\nabla \cdot V = \nabla \cdot \nabla \phi$, the discrete version of which is $\mathcal{D}V = \mathcal{D}\mathbf{G}\phi$.

The discrete form of Laplacian operator $\mathcal{L} := \mathcal{D}\mathbf{G}$ depends on computational grids. The commonly used grids are collocated, MAC, and vertex/node grids [28]. Fig. 2.1 shows the differences between the three grid types. On the collocated grid, the density, the pressure, and the velocities are all cell centered. On the MAC grid, the density and the pressure are cell centered, and the velocities are define on cell faces. On the vertex or node grid, the velocities are cell centered and the density and the pressure are defined at the vertices, or vice-versa. On the collocated grid, the stencil for \mathcal{L} is not the standard 5-point (for 2-D) stencil for the Laplacian, but rather an expanded 5-point stencil, which locally decouples a two-dimensional computational grid into four distinct subgrids [10]. Fig. 2.2 shows the standard and expanded 5-point stencils for the 2-D Laplacian. Specialized solution techniques are introduced to obtain solutions [10]. However, one problem is that the coupling of the pressure fields interacts poorly with source terms leading to instabilities for some application [4]. Alternatively, an approximate projection method, which uses a compact 5-point stencil (for 2-D) to approximate \mathcal{L} , is proposed, at the price of breaking Eq. (2.8) and thus making the velocity divergence a function of the truncation error [7]. While filtering is not typically done with approximate projections with nodal pressure, it is observed in [47] that the approximate projection method allows a non-physical oscillatory error to remain after the projection and thus a filter is needed to remove the non-physical mode.

Thus, we choose the MAC grid [46] over the collocated grid for two reasons: the velocity-pressure coupling and a standard 5-point (for 2-D) or 7-point (for 3-D) stencil for Laplacian \mathcal{L} . In this section, we present a second-order MAC projection method for solving the system of equations (2.1), (2.2), and (2.7), where the concentration equation (2.3) is replaced by the divergence constraint Eq. (2.7). The method is based

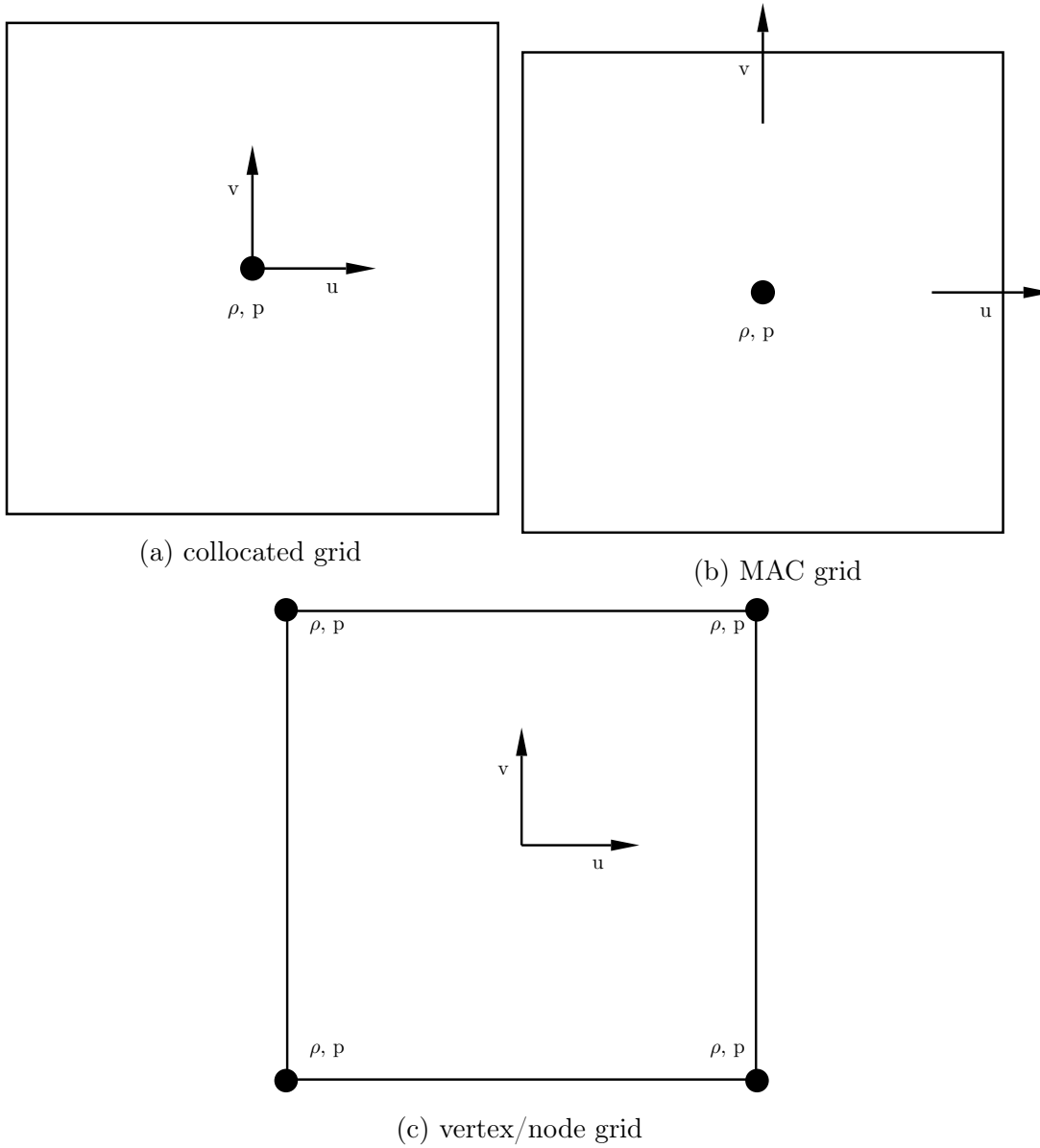


Figure 2.1: Plot of three grids with positioning of variables for 2-D. We denote the cell center as (i, j) , the cell faces as $(i + 1/2, j)$ and $(i, j + 1/2)$, and the cell vertices as $(i \pm 1/2, j \pm 1/2)$ and $(i \pm 1/2, j \mp 1/2)$. The MAC grid is used in the FrontTier simulations.

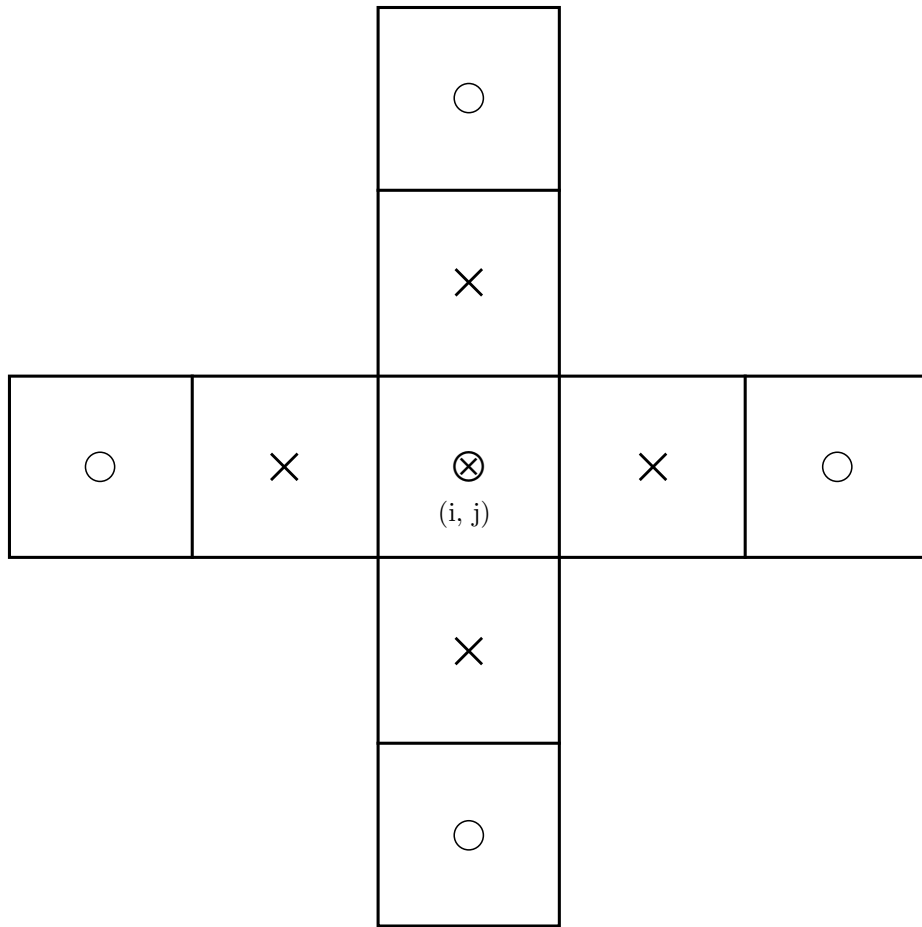


Figure 2.2: Plot of standard and expanded stencils for the two-dimensional Laplacian. The standard stencil consists of the grid (i, j) and 4 neighboring grids marked with " \times ", while the expanded stencil uses neighboring grids marked with " \circ ".

on the idea of [9, 10, 47, 82]. Assume the fluid states at time t^n are density ρ^n , velocity U^n , and pressure $p^{n-1/2}$, the algorithm for one complete step from time t^n to time $t^{n+1} = t^n + \Delta t$ is given briefly as below:

1. Extrapolate in time and space to obtain cell-center velocities $u_{ijk}^{n+1/2,W}$, $u_{ijk}^{n+1/2,E}$, $v_{ijk}^{n+1/2,N}$, $v_{ijk}^{n+1/2,S}$, $w_{ijk}^{n+1/2,B}$, and $w_{ijk}^{n+1/2,T}$. An upwinding procedure is then employed to uniquely determine $u_{ijk}^{n+1/2}$, $v_{ijk}^{n+1/2}$, and $w_{ijk}^{n+1/2}$ at cell centers [9]. The extrapolation step actually consists of two stages \hat{U} and \tilde{U} . On the MAC grid, \hat{U} and \tilde{U} are moderately modified from those originally introduced for the collocated grid [10]. It is worth pointing out that we apply a first-order monotonicity slope limiter to the normal derivatives [9], and compute the transverse derivatives defined in [65, 47] for improved stability.
2. Extrapolate in time and space to obtain cell-edge velocities. u and v are extrapolated to vertical edges, v and w to streamwise edges, u and w to spanwise edges. A upwind-like scheme is used to resolve the ambiguities, see [82] for a 2-D version of this scheme. Again, the extrapolation step includes two stages \hat{U} and \tilde{U} .
3. Compute the convection term $\left((U \cdot \nabla)U\right)^{n+1/2}$ using cell-center and cell-edge velocities. Three components of the convection term are placed on the u -, v -, and w -face, respectively. We define the convection term as

$$\begin{aligned}
& (uu_x + vv_y + ww_z)_{i+1/2,jk}^{n+1/2} = \\
& \quad \frac{u_{i+1,jk}^{n+1/2} + u_{ijk}^{n+1/2}}{2} \cdot \frac{u_{i+1,jk}^{n+1/2} - u_{ijk}^{n+1/2}}{\Delta x} \\
& + \frac{v_{i+1/2,j+1/2,k}^{n+1/2} + v_{i+1/2,j-1/2,k}^{n+1/2}}{2} \cdot \frac{u_{i+1/2,j+1/2,k}^{n+1/2} - u_{i+1/2,j-1/2,k}^{n+1/2}}{\Delta y} \\
& + \frac{w_{i+1/2,j,k+1/2}^{n+1/2} + w_{i+1/2,j,k-1/2}^{n+1/2}}{2} \cdot \frac{u_{i+1/2,j,k+1/2}^{n+1/2} - u_{i+1/2,j,k-1/2}^{n+1/2}}{\Delta z} \quad (2.9)
\end{aligned}$$

$$\begin{aligned}
& (uv_x + vv_y + ww_z)_{i,j+1/2,k}^{n+1/2} = \\
& \frac{u_{i+1/2,j+1/2,k}^{n+1/2} + u_{i-1/2,j+1/2,k}^{n+1/2}}{2} \cdot \frac{v_{i+1/2,j+1/2,k}^{n+1/2} - v_{i-1/2,j+1/2,k}^{n+1/2}}{\Delta x} \\
& + \frac{v_{i,j+1,k}^{n+1/2} + v_{ijk}^{n+1/2}}{2} \cdot \frac{v_{i,j+1,k}^{n+1/2} - v_{ijk}^{n+1/2}}{\Delta y} \\
& + \frac{w_{i,j+1/2,k+1/2}^{n+1/2} + w_{i,j+1/2,k-1/2}^{n+1/2}}{2} \cdot \frac{v_{i,j+1/2,k+1/2}^{n+1/2} - v_{i,j+1/2,k-1/2}^{n+1/2}}{\Delta z} \quad (2.10)
\end{aligned}$$

$$\begin{aligned}
& (uw_x + vw_y + ww_z)_{ij,k+1/2}^{n+1/2} = \\
& \frac{u_{i+1/2,j,k+1/2}^{n+1/2} + u_{i-1/2,j,k+1/2}^{n+1/2}}{2} \cdot \frac{w_{i+1/2,j,k+1/2}^{n+1/2} - w_{i-1/2,j,k+1/2}^{n+1/2}}{\Delta x} \\
& + \frac{v_{i,j+1/2,k+1/2}^{n+1/2} + v_{i,j-1/2,k+1/2}^{n+1/2}}{2} \cdot \frac{w_{i,j+1/2,k+1/2}^{n+1/2} - w_{i,j-1/2,k+1/2}^{n+1/2}}{\Delta y} \\
& + \frac{w_{ij,k+1}^{n+1/2} + w_{ijk}^{n+1/2}}{2} \cdot \frac{w_{ij,k+1}^{n+1/2} - w_{ijk}^{n+1/2}}{\Delta z} \quad (2.11)
\end{aligned}$$

4. Extrapolate in only time to obtain cell-face velocities $u_{i+1/2,j,k}^{n+1/2}$, $v_{i,j+1/2,k}^{n+1/2}$, and $w_{ij,k+1/2}^{n+1/2}$ on the u -, v -, and w -face, respectively. Perform a MAC-type projection to enforce the divergence constraint Eq. (2.7) on the face velocities [47]. We solve the following equation for ϕ

$$\left(\mathcal{D} \frac{1}{\rho^n} \mathbf{G} \phi \right)_{ijk} = \mathcal{D} U_{ijk}^{n+1/2} - S_{ijk}^n \quad (2.12)$$

where $\left(\mathcal{D} \frac{1}{\rho^n} \mathbf{G} \phi \right)_{ijk}$ can be discretized as a density-weighted compact 7-point

stencil, S is defined in Eq. (2.7), $\mathcal{D}U_{ijk}^{n+1/2}$ is computed using cell-face velocities

$$\begin{aligned}\mathcal{D}U_{ijk}^{n+1/2} = & \frac{u_{i+1/2,jk}^{n+1/2} - u_{i-1/2,jk}^{n+1/2}}{\Delta x} \\ & + \frac{v_{i,j+1/2,k}^{n+1/2} - v_{i,j-1/2,k}^{n+1/2}}{\Delta y} \\ & + \frac{w_{ij,k+1/2}^{n+1/2} - w_{ij,k-1/2}^{n+1/2}}{\Delta z}\end{aligned}\quad (2.13)$$

To solve the Poisson equation Eq. (2.12) with pure Neumann boundary condition, we adopt the corresponding sparse linear system solver that is accessible from PETSc [8]. This solver uses multigrid [15] to solve the elliptic problem. In case of failure, Generalized Minimal Residual (GMRES) method [78] is used instead.

Then update face velocities as follows:

$$u_{i+1/2,jk}^{n+1/2} \leftarrow u_{i+1/2,jk}^{n+1/2} - \frac{\phi_{i+1,jk} - \phi_{ijk}}{\rho_{i+1/2,jk}^n \Delta x} \quad (2.14)$$

$$v_{i,j+1/2,k}^{n+1/2} \leftarrow v_{i,j+1/2,k}^{n+1/2} - \frac{\phi_{i,j+1,k} - \phi_{ijk}}{\rho_{i,j+1/2,k}^n \Delta y} \quad (2.15)$$

$$w_{ij,k+1/2}^{n+1/2} \leftarrow w_{ij,k+1/2}^{n+1/2} - \frac{\phi_{ij,k+1} - \phi_{ijk}}{\rho_{ij,k+1/2}^n \Delta z} \quad (2.16)$$

It is noted that a lagged source term S^n is used in the projection, since the values of $\rho^{n+1/2}$ are not available so far.

5. Extrapolate in time and space to obtain cell-face densities $\rho_{i+1/2,jk}^{n+1/2}$, $\rho_{i,j+1/2,k}^{n+1/2}$, and $\rho_{ij,k+1/2}^{n+1/2}$. During the extrapolation procedure that consists of two stages $\hat{\rho}$ and $\tilde{\rho}$, ghost cells are introduced to compute both the normal and transverse derivatives for ρ^n on cells near the tracked front (i.e. irregular cells), in order to minimize numerical mass diffusion. More details of the front tracking and ghost cell method are available in Sec. 2.1.3. We then apply the upwinding procedure

to eliminate the ambiguities based on the relevant cell-face velocities.

6. Compute the mass flux $\left(\nabla \cdot (\rho U)\right)_{ijk}^{n+1/2}$ using cell-face velocities and densities

$$\begin{aligned} \left(\nabla \cdot (\rho U)\right)_{ijk}^{n+1/2} &= \frac{(\rho u)_{i+1/2,jk}^{n+1/2} - (\rho u)_{i-1/2,jk}^{n+1/2}}{\Delta x} \\ &\quad + \frac{(\rho v)_{i,j+1/2,k}^{n+1/2} - (\rho v)_{i,j-1/2,k}^{n+1/2}}{\Delta y} \\ &\quad + \frac{(\rho w)_{ij,k+1/2}^{n+1/2} - (\rho w)_{ij,k-1/2}^{n+1/2}}{\Delta z} \end{aligned} \quad (2.17)$$

Advance the density to ρ^{n+1} using Crank-Nicolson differencing of Eq. (2.1)

$$\rho_{ijk}^{n+1} = \rho_{ijk}^n - \Delta t \left(\nabla \cdot (\rho U)\right)_{ijk}^{n+1/2} \quad (2.18)$$

Compute the time-centered source term $S^{n+1/2}$ using time-centered density $\rho^{n+1/2} := (\rho^n + \rho^{n+1})/2$.

7. Perform another MAC-type projection on face velocities as Step 4 using the source term $S^{n+1/2}$, and update cell-face velocities, in order to keep second-order accuracy in time. Recompute cell-face densities as Step 5, since we have new cell-face velocities for the upwinding procedure. Recompute the mass flux and ρ^{n+1} as Step 6, using updated cell-face velocities and densities. Update time-centered density $\rho^{n+1/2}$ and compute the dynamic viscosity $\mu^{n+1} = \rho^{n+1}\nu$.
8. Compute an intermediate velocity field $U^* = (u^*, v^*, w^*)$, which is an approximation to U^{n+1} , but usually does not satisfy the divergence constraint. U^* are

updated by solving

$$U^* = U^n + \Delta t \left[- \left((U \cdot \nabla) U \right)^{n+1/2} + \vec{g} - \frac{1}{\rho^{n+1/2}} \nabla p^{n-1/2} + \frac{1}{\rho^{n+1/2}} \frac{\nabla \cdot \tau^* + \nabla \cdot \tau^n}{2} \right] \quad (2.19)$$

on the u -, v -, and w -faces, respectively. Here, $\nabla \cdot \tau^*$ and $\nabla \cdot \tau^n$ are the viscous stress tensors for (μ^{n+1}, U^*) and (μ^n, U^n) , with the latter serving as a source term. It is worth mentioning that $\left((U \cdot \nabla) U \right)^{n+1/2}$, $\nabla p^{n-1/2}$, and $\nabla \cdot \tau$ have their three components defined on the u -, v -, and w -faces respectively for MAC grid. Then perform a MAC projection to enforce the divergence constraint on U^{n+1} .

We solve

$$\left(\mathcal{D} \frac{1}{\rho^{n+1/2}} \mathbf{G} \phi \right)_{ijk} = \frac{1}{\Delta t} (\mathcal{D} U^* - S^{n+1})_{ijk} \quad (2.20)$$

for ϕ , where $\mathcal{D} U_{ijk}^*$ is computed as

$$\begin{aligned} \mathcal{D} U_{ijk}^* &= \frac{u_{i+1/2,jk}^* - u_{i-1/2,jk}^*}{\Delta x} \\ &+ \frac{v_{i,j+1/2,k}^* - v_{i,j-1/2,k}^*}{\Delta y} \\ &+ \frac{w_{ij,k+1/2}^* - w_{ij,k-1/2}^*}{\Delta z} \end{aligned} \quad (2.21)$$

Update the velocity and pressure by

$$u_{i+1/2,jk}^{n+1} = u_{i+1/2,jk}^* - \frac{\Delta t (\phi_{i+1,jk} - \phi_{ijk})}{\rho_{i+1/2,jk}^{n+1/2} \Delta x} \quad (2.22)$$

$$v_{i,j+1/2,k}^{n+1} = v_{i,j+1/2,k}^* - \frac{\Delta t (\phi_{i,j+1,k} - \phi_{ijk})}{\rho_{i,j+1/2,k}^{n+1/2} \Delta y} \quad (2.23)$$

$$w_{ij,k+1/2}^{n+1} = w_{ij,k+1/2}^* - \frac{\Delta t (\phi_{ij,k+1} - \phi_{ijk})}{\rho_{ij,k+1/2}^{n+1/2} \Delta z} \quad (2.24)$$

$$p_{ijk}^{n+1/2} = p_{ijk}^{n-1/2} + \phi_{ijk} \quad (2.25)$$

9. Propagate the tracked interface using U^{n+1} . The interface is propagated in a Lagrangian manner by solving the ODE

$$\frac{d\mathbf{x}_f}{dt} = \mathbf{V}_n(\mathbf{x}_f) \quad (2.26)$$

where \mathbf{x}_f represent the marker points on the tracked interface, $\mathbf{V}_n(\mathbf{x}_f)$ is the normal velocity at \mathbf{x}_f , which is calculated by interpolation from the fixed grid points to the interface marker point by use of bilinear interpolation [85]. Apply the high-order mesh smoothing [50, 76, 23, 89], surface redistribution, and local grid based (LGB) untangling [29, 14] to the tracked interface, if necessary.

2.1.3 Front Tracking and Ghost Cell Method

We use a front tracking algorithm [37, 36, 61, 14] which minimizes numerical diffusion, especially in the equations where it is typically the largest: thermal and concentration diffusion. The front tracking controls, or limits, diffusion by tracking a sharp interface for immiscible mixing flows or steep thermal/concentration gradient for miscible mixing flows, the latter defines the tracked interface for the hot/cold water FrontTier simulations. At the discrete level, the interface is described as a geometrical manifold represented by a set of topologically linked marker points. In 3-D, the interface consists of POINTs/NODEs, CURVEs/BONDs, TRIANGLEs, SURFACEs and others [39, 29], see Fig. 2.3. For a flowchart for the front tracking algorithm, see Fig. 2.4 [29].

In front tracking method, each species is assigned a unique global component. The front tracking method provides the capacity of calculating the component at a given point, using the point position and the orientation of surfaces, as seen in Fig. 2.3. At

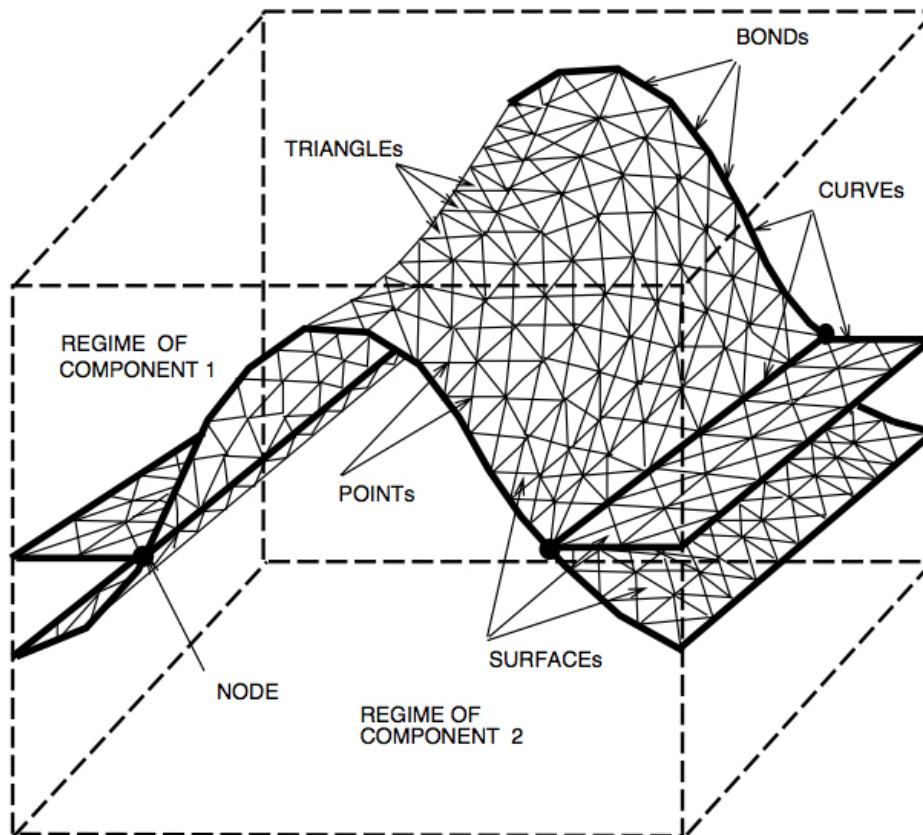


Figure 2.3: Plot of the basic geometrical data structures employed by the front tracking method for three dimensions.

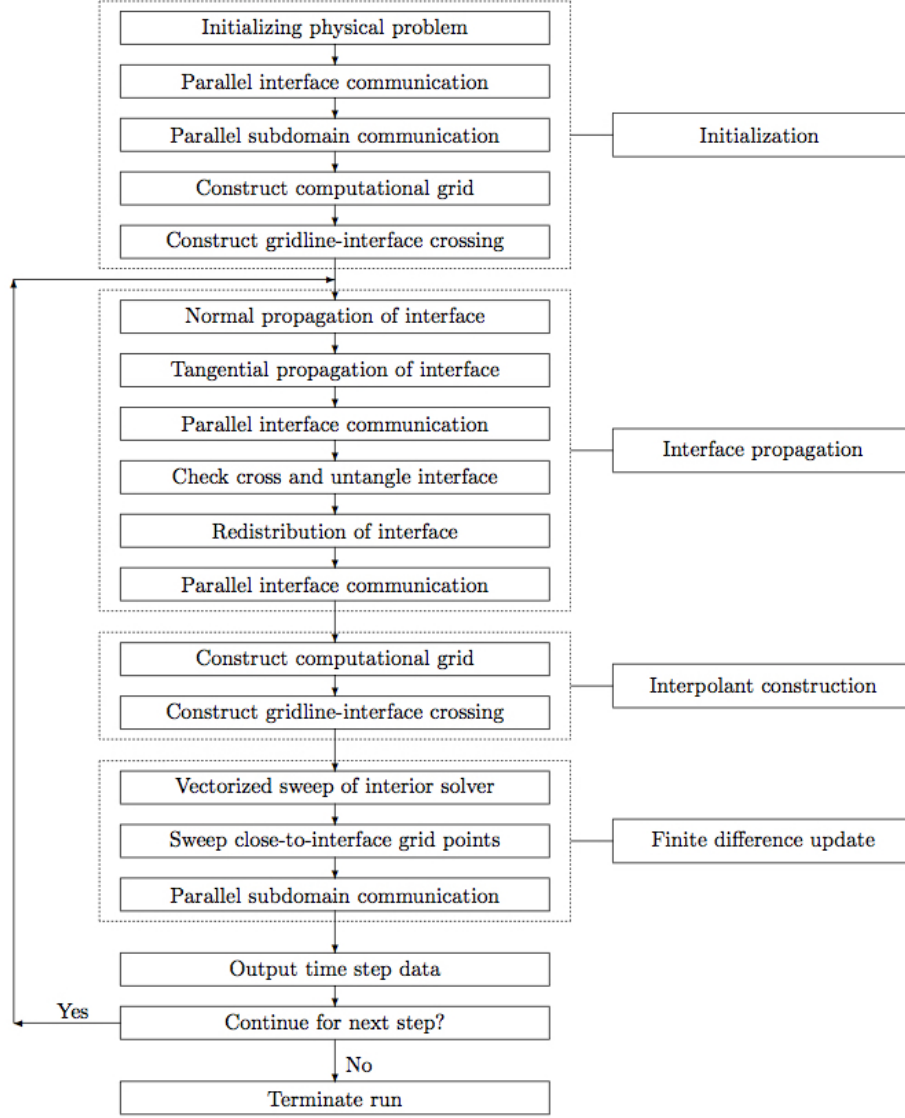


Figure 2.4: Flowchart for the front tracking framework. To follow the best practices, the interface/front library is developed/debugged/tested/maintained independently from a variety of physics application libraries in FronTier.

the grid level, the components are defined at cell centers and updated every time step as the interface propagates.

Based on the component information, we can identify the irregular cells, whose components are different from the component of either its left or right neighbors. The irregular cell is defined in a direction-splitting fashion, meaning that a cell that is recognized as irregular in the west direction may be regular in the other directions, see Fig. 2.5. For each irregular cell, ghost cells are employed to calculate the advective derivatives of discontinuous fluid states. In the hot/cold water FronTier simulations, since we do not solve the concentration equations, the only discontinuous fluid state across the interface is the density. Also, since the hot/cold water experiment and simulations involve two species in total, the front tracking uses two components, denoted as black and white components. A simple constant extrapolation scheme is employed to construct ghost densities for ghost cells. For example, to compute the advective derivatives of the density on the irregular cell (i, j) , the ghost density ρ_{ij} is used as the real density on the west and north (ghost) cells. In contrast, the east and south (normal) cells use their original densities, as shown by Fig. 2.5.

We note that a second-order projection method for variable-density flows was presented in [73]. In this method, an approximate projection formulation is employed, and the boundary between the fluids is tracked with a second-order, volume-of-fluid (VOF) interface tracking algorithm. A detailed comparison between this method and our incompressible tracking method can be very useful, which will be made in the future work. It is worth mentioning that a comparison study on the performance of several interface methods, e.g. the LGB/GF/GB front tracking, level set method [69], VOF [48] and other methods, is available in [29].

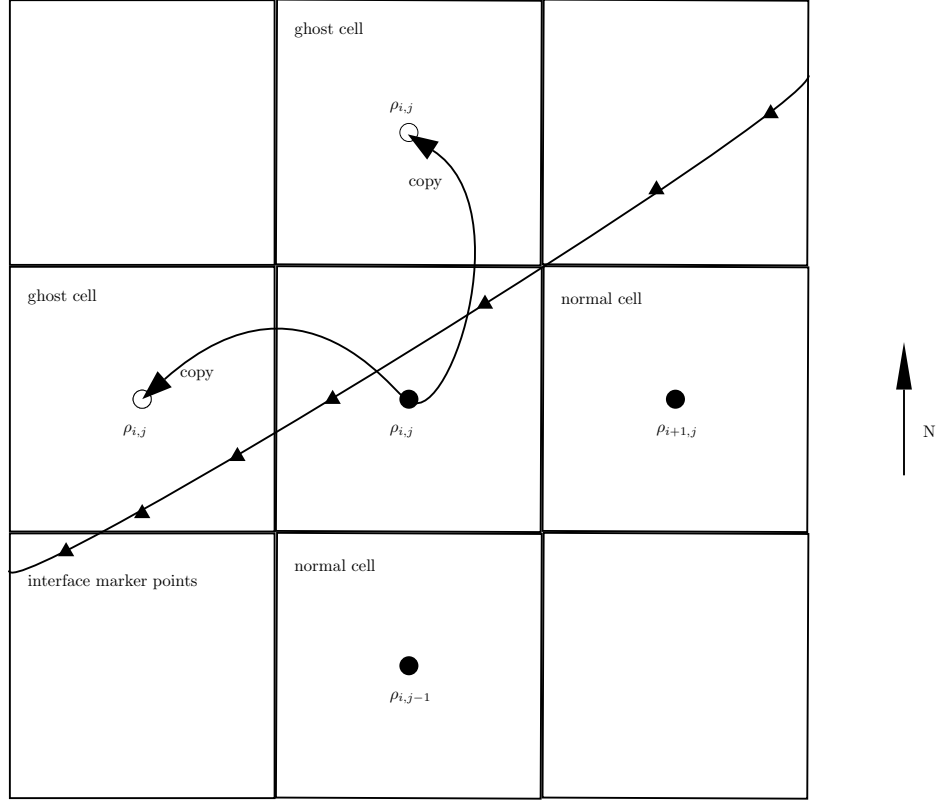


Figure 2.5: Plot of a two-dimensional irregular cell (i, j) , with the black component. The cell is irregular w.r.t. its west and north neighbors, however, it is regular w.r.t. its east and south neighbors. The ghost density ρ_{ij} is used as the real density on the west and north (ghost) cells, but the east and south (normal) cells use their original densities $\rho_{i+1,j}$ and $\rho_{i,j-1}$.

2.1.4 Simulation Parameters, Initial and Boundary Conditions

We use the same physical parameters as [67], except that $\mu_1 = 0.011$ g/cm s and $\mu_2 = 0.009$ g/cm s. A half-size computational domain $28.8 \times 9 \times 24$ cm³ is chosen by the FronTier simulations, in order to reduce the total computational cost, but the change retains the longest wave lengths modeled by the single Miranda grid. The FronTier simulation uses three grids, which are two, four and eight times coarser respectively than the single Miranda grid. See Table 2.1.

FronTier simulations are initialized with the same initial density, velocity and interfacial perturbation as [67], except that:

1. The width of initial diffusion layer ε is initialized to be $\varepsilon = 0.174$ cm instead of 0.3 cm used by the Miranda simulation. The value of ε is properly chosen such that three FronTier simulations can meet the first available experimental data point for the molecular mixing parameter θ , as seen in Fig. 3.4.
2. The velocity potential field is defined similar to that used in [27]

$$\psi(\mathbf{x}, t = 0) = \text{sgn}(z) \cdot \text{Re} \sum_{k_x=k_{min}}^{k_{max}} \frac{\hat{w}(k_x)}{k_x} \begin{cases} e^{ik_x x - k_x z} & \text{if } z \geq 0 \\ e^{ik_x x + k_x z} & \text{if } z < 0 \end{cases} \quad (2.27)$$

where $\text{sgn}(\cdot)$ represents the sign function. The formulation of the velocity potential field given in [67] seems to leave out the sign function for some unknown reason.

In FronTier simulations, the initial density field is modeled as [24]

$$\rho(\mathbf{x}, t = 0) = \frac{\rho_1 + \rho_2}{2} + \frac{\rho_1 - \rho_2}{2} \text{erf} \left(\frac{z + \zeta(x, y)}{\varepsilon/2} \right) \quad (2.28)$$

Table 2.1: Table of simulation parameters used in the FronTier simulations

Parameter	Value
ρ_1	0.9985986 g/cm ³
ρ_2	0.9970479 g/cm ³
A	7.7704×10^{-4}
g	981 cm/s ²
μ_1	0.011 g/cm s
μ_2	0.009 g/cm s
$\nu := (\mu_1 + \mu_2)/(\rho_1 + \rho_2)$	0.010022 cm ² /s
Sc	7
D	1.431688×10^{-3} cm ² /s
Computational domain $L_x \times L_y \times L_z$	$28.8 \times 9 \times 24$ cm ³
Grid resolution of coarse grid	$0.2 \times 0.2 \times 0.2$ cm ³
Grid resolution of medium grid	$0.1 \times 0.1 \times 0.1$ cm ³
Grid resolution of fine grid	$0.05 \times 0.05 \times 0.05$ cm ³
Initial longest wave length in x -direction	28.8 cm
Initial shortest wave length in x -direction	0.6 cm
Number of initial normal modes in x -direction	25
Initial longest wave length in y -direction	9 cm
Initial shortest wave length in y -direction	0.4 cm
Number of initial normal modes in y -direction	36
Width of initial diffusion layer ε	0.174 cm

where ρ_1 and ρ_2 are the densities of cold and hot water, $\varepsilon = 0.174$ cm is the width of the initial diffusion layer separating two fluids, $\text{erf}(\cdot)$ is the error function, and $\zeta(x, y)$ is the 2-D initial interfacial perturbation, which is modeled as the superimposition of a set of discrete wave numbers and mode phases and the experimentally measured mode amplitudes in the x - and y -directions [68, 67]

$$\zeta(x, y) = \text{Re} \sum_{k_x=k_{min}}^{k_{max}} A(k_x) e^{ik_x x} + \text{Re} \sum_{k_y=k_{min}}^{k_{max}} A(k_y) e^{ik_y y} \quad (2.29)$$

where $\mathbf{k} = (k_x, k_y) := (2\pi/\lambda_x, 2\pi/\lambda_y)$ are the wave numbers, $A(k_x)$ and $A(k_y)$ are the mode amplitudes in the x - and y -directions.

The upper bound of the wave lengths $\lambda = (\lambda_x, \lambda_y)$ in the x - and y -directions that can be supported by numerical simulations is determined by the computational domain size $L_x \times L_y$, i.e. $\lambda_{max} = (L_x, L_y) = (28.8, 9.0)$ cm. The lower bound is determined by the grid resolution (Nyquist limit), i.e. $\lambda_{min} = (2\Delta x, 2\Delta y)$. Since the grid resolution of the FronTier coarse grid is $0.2 \times 0.2 \times 0.2$ cm³, a uniform lower bound $\lambda_{min} = (0.4, 0.4)$ cm is applied to three FronTier simulations. Given the upper/lower bound of the wave lengths, we take 25 normal modes in the x -direction, with the wave lengths ranging from 0.6 cm to 28.8 cm; and in the y -direction, we choose 36 modes, whose wave lengths are between 0.4 cm and 9 cm. As already emphasized, FronTier simulations use the same longest wave lengths as the Miranda. The mode amplitudes $A(k_x)$ and $A(k_y)$ are measured from the hot/cold water experiment. Phases for each normal mode are randomly generated in $[-\pi, \pi]$. For the set of wave numbers $\mathbf{k} = (k_x, k_y)$ and mode amplitudes $A(k_x)$ and $A(k_y)$ used in FronTier simulations, see Table 2.2. The visualization of the initial density and two-dimensional interfacial perturbation on FronTier medium grid is shown in Fig. 2.6 and 2.7, respectively.

Table 2.2: Table of wave numbers $\mathbf{k} = (k_x, k_y)$ and mode amplitudes $A(\mathbf{k})$ and \hat{w} in FronTier simulations

k_x	$A(k_x)$	$\hat{w}(k_x)$	k_y	$A(k_y)$
0.218165972	1.1780e-05	0.0215724	0.698139183	6.6591e-03
0.436331944	3.1166e-05	0.0473242	1.047204739	1.1534e-02
0.654497917	2.1399e-05	0.0353649	1.396270294	1.1534e-02
0.872663889	1.8625e-05	0.0168830	1.745335850	7.7761e-03
1.090829861	1.7472e-05	0.0150621	2.094401405	3.4776e-03
1.308995833	1.6659e-05	0.0132103	2.443466961	4.4444e-03
1.527161806	2.5808e-05	0.0153490	2.792532516	3.6473e-03
1.745327778	5.7708e-05	0.0166226	3.141598072	1.9774e-03
1.963493750	4.7118e-05	0.0381349	3.490663628	6.9552e-04
2.181659722	5.5251e-05	0.0590783	3.839729183	4.9589e-04
2.399825694	4.9976e-05	0.0463931	4.188794739	1.2539e-03
2.617991667	4.0806e-05	0.0300274	4.537860294	2.3756e-03
2.836157639	3.3318e-05	0.0345326	4.886925850	2.4590e-03
3.054323611	2.6862e-05	0.0332452	5.235991405	1.1707e-03
3.272489583	3.5339e-05	0.0274995	5.585056961	6.6591e-04
3.490655556	3.7250e-05	0.0258643	5.934122516	4.4895e-04
3.708821528	3.9068e-05	0.0247142	6.283188072	1.3318e-03
3.926987500	3.7250e-05	0.0258643	6.632253628	1.7618e-03
5.672315278	4.2472e-05	0.0208873	6.981319183	1.9047e-03
5.890481250	4.4075e-05	0.0215724	7.330384739	2.9096e-03
6.108647222	4.3120e-05	0.0222363	7.679450294	3.3597e-03
6.544979167	2.5808e-05	0.0215724	8.028515850	3.1104e-03
7.853975000	2.1720e-05	0.0107862	8.377581405	3.2375e-03
8.726638889	2.5537e-05	0.0078153	8.726646961	3.5351e-03
10.47196667	1.8625e-05	0.0076270	9.075712516	3.0450e-03
#	#	#	9.424778072	1.9047e-03
			9.773843628	1.2047e-03
			10.12290918	8.5183e-04
			10.47197474	1.0238e-03
			10.82104029	1.4197e-03
			11.17010585	1.6557e-03
			11.86823696	1.5158e-03
			12.21730252	1.6557e-03
			13.96263029	2.9780e-03
			15.70795807	2.3756e-03
			16.05702363	2.6178e-03

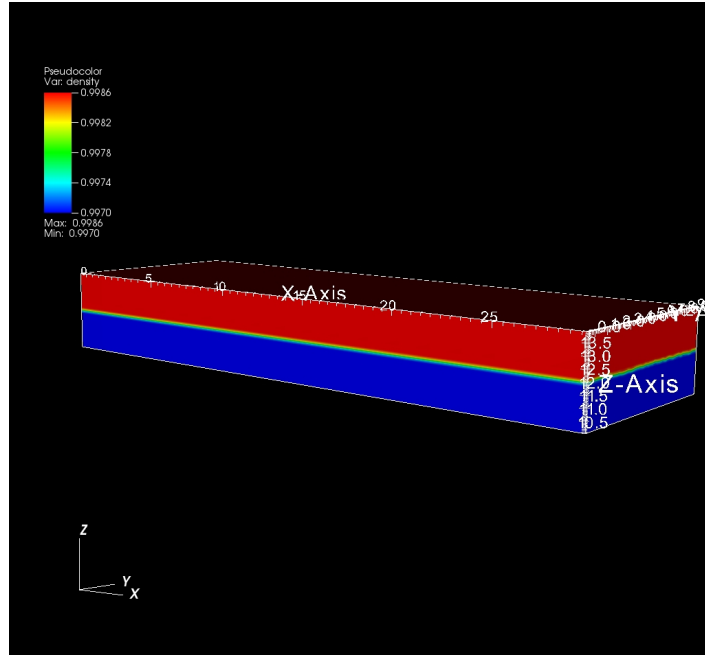


Figure 2.6: Plot of the initial density field on the FronTier medium grid. The width of the initial diffusion layer $\varepsilon = 0.174$ cm, so that three FronTier simulations can meet the first available experimental data point for the molecular mixing parameter θ . For better visual effect, a partial computational domain is presented here.

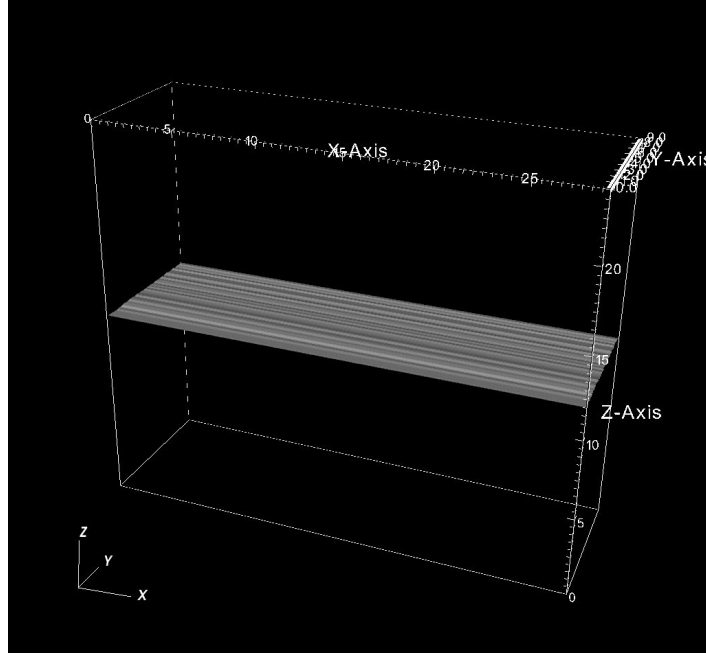


Figure 2.7: Plot of the initial two-dimensional interfacial perturbation $\zeta(x, y)$ on the FronTier medium grid. $\zeta(x, y)$ is modeled using the interfacial perturbation spectra from the hot/cold water channel experiment in the x - and y -directions.

The initial velocity field is the superimposition of the gradient of the velocity potential field ψ that is defined as (2.27) and a diffusion velocity

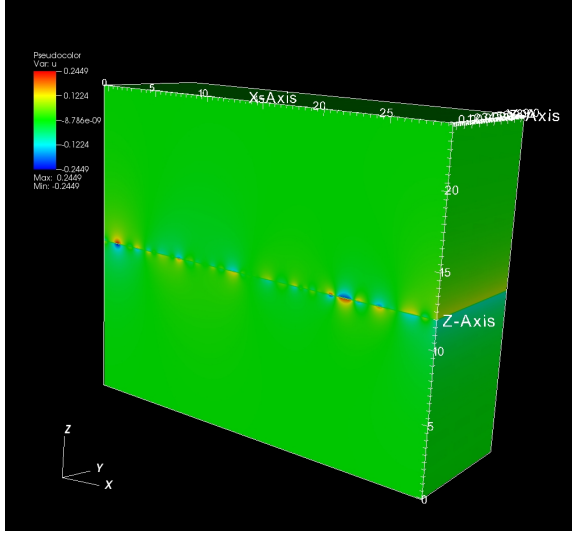
$$U(\mathbf{x}, t = 0) = \nabla\psi|_{t=0} - \frac{D}{\rho}\nabla\rho|_{t=0} \quad (2.30)$$

where $D = \nu/\text{Sc}$ is the binary diffusivity, $\text{Sc} = 7$ is the Schmidt number. Given that $\nabla\psi$ is divergence free everywhere except on the vortex sheet (i.e. the midplane $z = 0$), it is easy to verify that $U(\mathbf{x}, t = 0)$ satisfies the divergence constraint (2.7) everywhere except on the mid-plane. However, it is observed that U satisfies (2.7) globally after one time step. For the set of wave numbers k_x and mode amplitudes $\hat{w}(k_x)$ used for defining ψ , see Table 2.2.

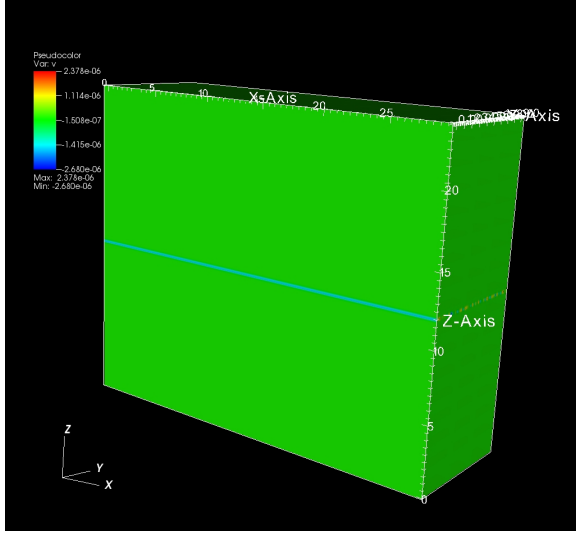
Observations from the water channel experiment indicates the existence of both u (vertical) and w (streamwise) velocity fluctuations and thus the existence of oscillating shearing zones between the upper and lower flows, consistent with the vortex-sheet type velocity initialization used in the Miranda and FronTier simulations. The shearing motion is captured by the initial u velocity field, which is discontinuous across the midplane $z = 0$ of the mixing zone due to the sign function in the potential field ψ . In contrast, the initial v and w velocities are continuous over the entire computational domain. While the initial v (spanwise) velocity is negligible everywhere, with the maximum value in the order of magnitude $O(10^{-6})$ cm/s, both u and w velocities take their maximum values at the midplane $z = 0$ and exponentially decay with vertical distance from the midplane $z = 0$, as shown in Fig. 2.8.

The initial pressure satisfies $\nabla p = 0$. We take $p = 0$ and iterate on the first time step to obtain a good approximation to the pressure $p^{1/2}$.

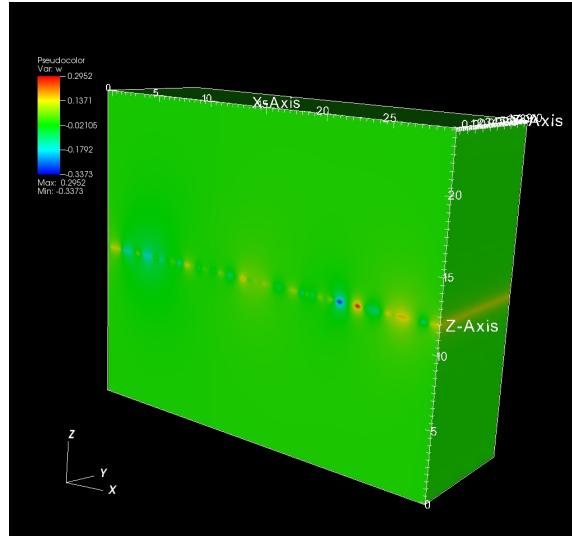
Periodic boundary conditions are applied in the x - and y -directions, with no-slip



(a) initial streamwise velocity u



(b) initial spanwise velocity v



(c) initial vertical velocity w

Figure 2.8: Plots of the initial velocity field on the FronTier medium grid, where u , v , and w are streamwise, spanwise, and vertical velocities, respectively. The v velocity is negligible everywhere. Both u and w velocities take their maximum values at the midplane and exponentially decay with vertical distance from the midplane.

walls at the top and bottom boundaries for the density and velocity, where $\rho = \rho_1$ and ρ_2 on the top and bottom boundary, and $U = 0$ for both boundaries. The homogeneous Neumann boundary condition is imposed on ϕ , i.e. $(\partial\phi/\partial z)|_{\text{bdry}} = 0$.

2.2 A New FronTier Package

A front is presented as an unstructured triangulation of a smooth surface (folds and self intersections can be supported, but are not discussed here). The triangles and adjacency information are stored. X. Jiao and students [50, 76, 23] have produced a new interface package, replacing our older interface software. For each front point (i.e., a triangle vertex), we find a discrete local coordinate patch, or stencil, of adjacent triangles and extending a prescribed distance. Over this stencil, the interface is represented by a height function h relative to the tangent plane at the central vertex. The height function is approximated as C^k polynomials, leading to equations for the polynomial coefficients. The stencil is chosen too large, so that the equations are over determined, and they are then solved approximately by least squares. The result is a robust description of the curvilinear surface, which survives poor triangulation. From this C^k description, all differential geometry operations can be derived in a straightforward if tedious manner, including formulas for normal, curvature and quadrature, with the desired order of accuracy.

Chapter 3

Results and Discussion

We first display the plots of the tracked interfaces for selected early- and late-times. Our simulations are qualitatively consistent with the experiment and Miranda simulation. Then we show the width $h(t)$ of the mixing zone, as a function of t , comparing FronTier and Miranda simulations to experimental data. All simulations show satisfactory comparison, with the FronTier simulations perhaps slightly improved over Miranda. This is in spite of the coarser grids (two, four and eight times coarser). The lower resolution only affects the convergence. We also show three statistical second moments of the flow, the mixing parameter θ , and u and w velocity variances at the midplane of the mixing zone. Our simulations achieve excellent agreement with two of these and partial agreement with the third. Followed is the justification of the omission of SGS terms for FronTier simulations. The section ends with a discussion of our statistical results.

3.1 Evolution of the Rayleigh-Taylor Mixing Zone

To facilitate comparisons between the experiment and Miranda and FronTier simulations, we introduce a dimensionless time τ defined as [81, 25, 74]

$$\tau = \sqrt{\frac{gA}{H}} \cdot t \quad (3.1)$$

where A is the Atwood number, g is the gravity, and H is the vertical height of the water channel [67]. We display the plots of the tracked interfaces for the FronTier medium grid simulation at the dimensionless time $\tau = 0.21, 0.5, 1.01$, and 1.5 . Careful qualitative observations indicate that the tracked interfaces look similar to the $f_1 = 0.5$ volume fraction isosurfaces in the Miranda simulation, as shown in Fig. 3.2. The simulation results are qualitatively consistent with the development of the RT mixing zone observed over a dimensionless time interval $0 < \tau < 0.8$ in the water channel experiment, as seen in Fig. 3.1.

It is observed in the experiment that the initial growth of the RT unstable mixing zone is dominated by the anisotropic initial velocity perturbations. This is also noted in the Miranda and FronTier simulations, where the early-time growth of the mixing zone resembles the early-time growth in 2-D simulations. This can be clearly seen in the early-time evolution of the RT mixing layer, see Fig. 3.2a - 3.2d.

In the y -direction or spanwise direction, the experiment, Miranda and FronTier simulations exhibit the "riblike" structures along the cylindrical structures, as seen in Fig. 3.2c and 3.2d. Since there are no velocity perturbations in the y -direction, such riblike structures are due to the interfacial perturbations in this direction.

The nonlinear transition to a more complicated 3-D RT mixing zone is observed in

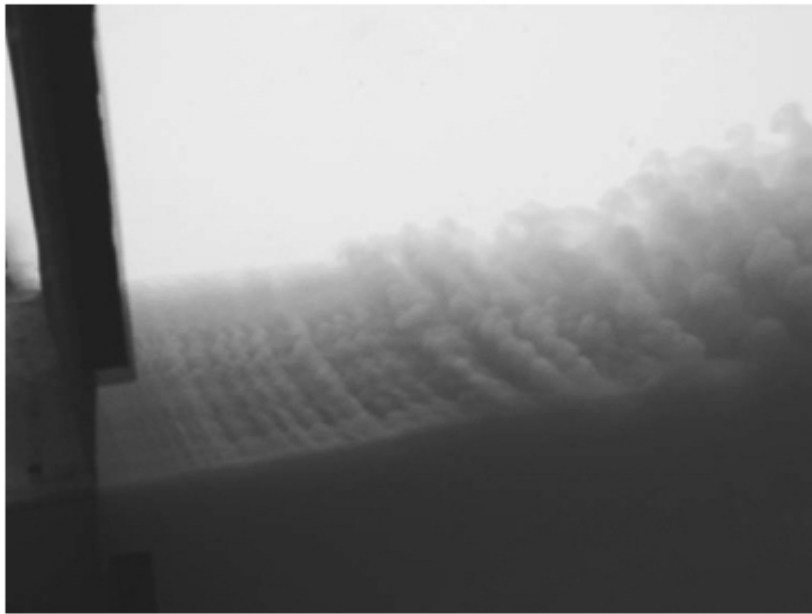


Figure 3.1: Photograph of the early-time development of the mixing zone in the water channel experiment. The mean flow is from left to right, corresponding to a dimensionless time interval $\tau \in [0, 0.8]$.

the Miranda and FronTier simulations at $\tau \approx 1$, as shown by Fig. 3.2e and 3.2f. The bubbles and spikes appear to better resemble spherical than cylindrical morphology by $\tau \approx 1$. The Miranda and FronTier medium/fine simulations reach a dimensionless time $\tau \approx 1.5$, while the FronTier coarse grid continues until $\tau \approx 1.8$.

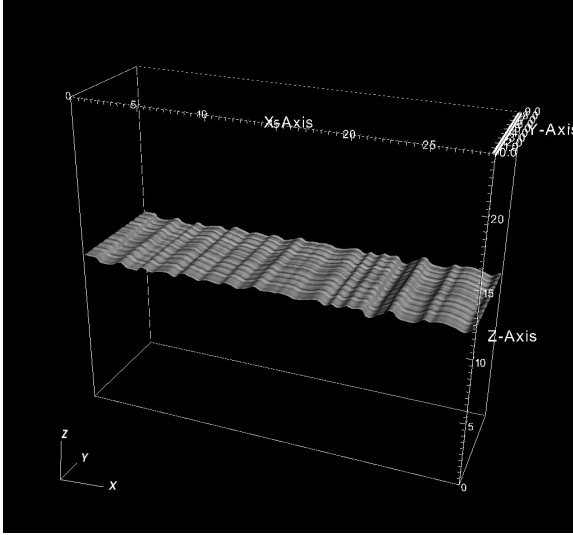
3.2 Mixing Zone Growth

The mixing zone width is by convention determined by the distance between the penetration of the bubble and spike fronts into each respective fluid. Consistent with the water channel experiment and Miranda simulation, the bubble and spike penetrations are defined by the 5% and 95% thresholds for the volume fraction f . At late times, under certain idealized conditions, the mixing zone growth rate can be characterized by the dimensionless self-similar parameter α , defined as

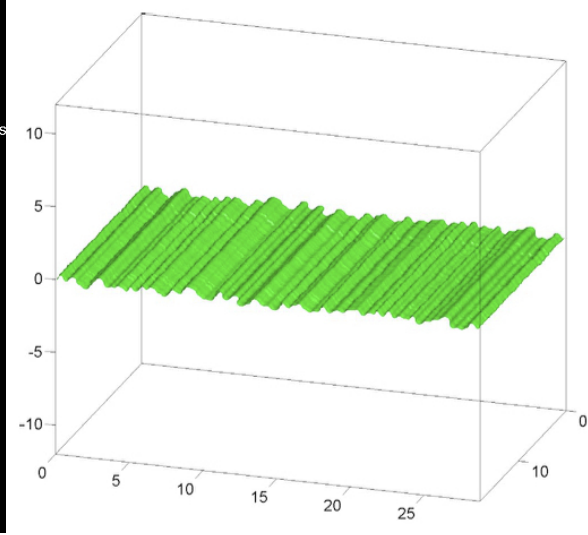
$$h(t) := h_b(t) + h_s(t) = \alpha A g t^2 \quad (3.2)$$

where h_b and h_t represent bubble and spike front widths, A is the Atwood number, g is the gravity.

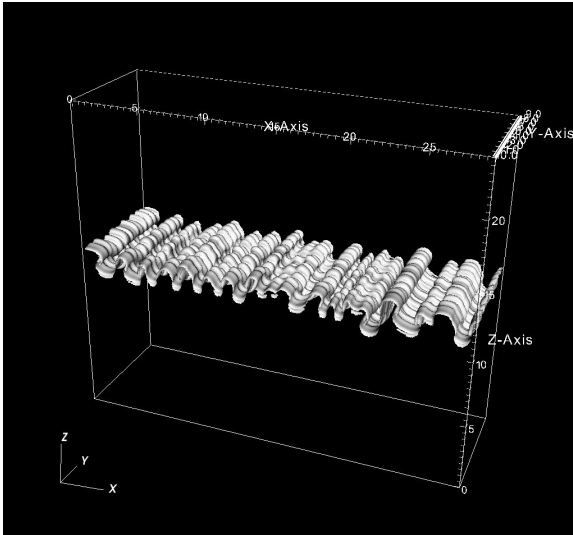
At earlier times, the slower simulation growth is observed for the Miranda and FronTier simulations, which is likely due to incorrect modeling of the initial density or velocity or interfacial perturbations. The growth parameter for bubbles α_b inferred from the FronTier simulations appears to approach the experimental value $\alpha_{b, \text{exp}} \approx 0.07$ for late times, as shown in Fig. 3.3. Overall, all simulations show satisfactory comparison, with the FronTier simulations perhaps slightly improved over Miranda. This is in spite of the coarser grids (two, four and eight times coarser respectively than the single



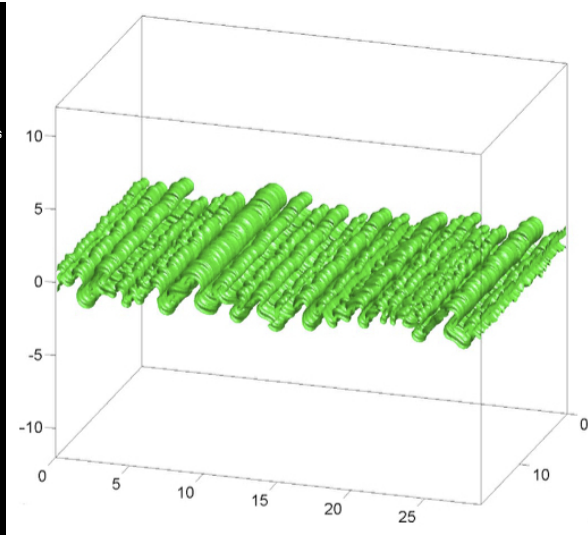
(a) $\tau = 0.21$ - FronTier



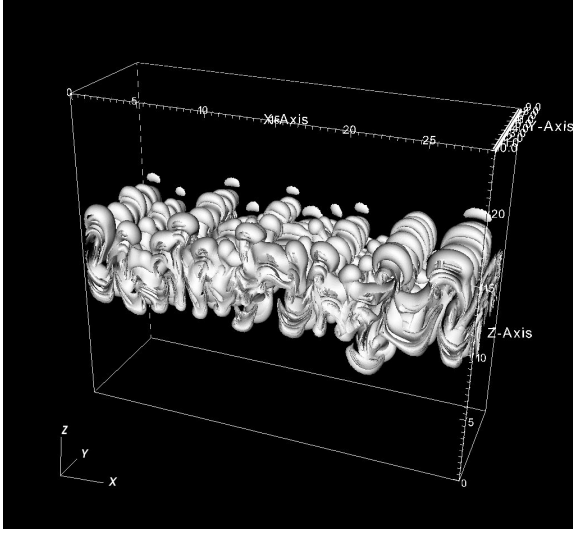
(b) $\tau = 0.21$ - Miranda



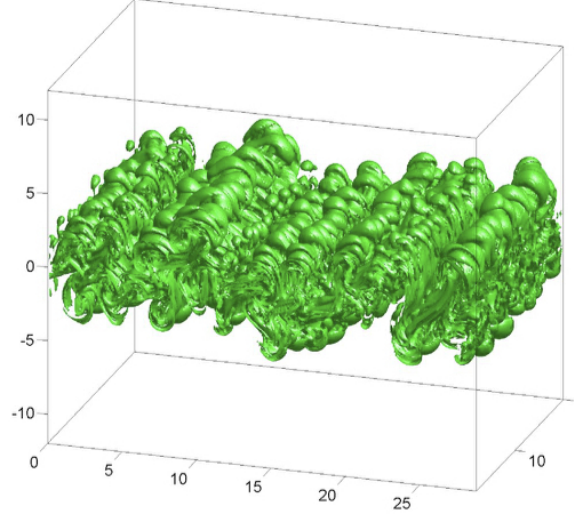
(c) $\tau = 0.5$ - FronTier



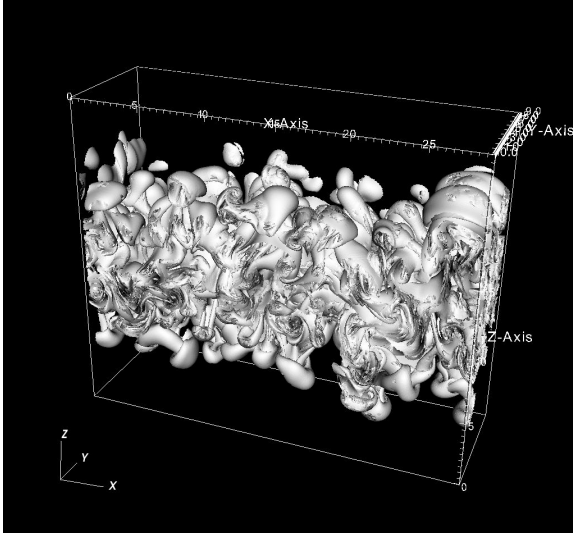
(d) $\tau = 0.5$ - Miranda



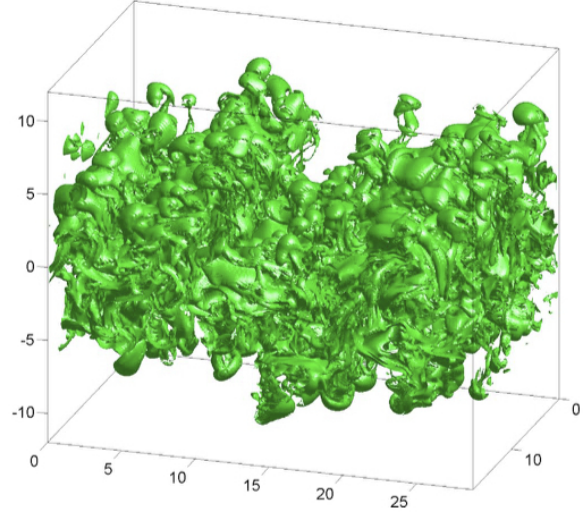
(e) $\tau = 1.01$ - FronTier



(f) $\tau = 1.01$ - Miranda



(g) $\tau = 1.5$ - FronTier



(h) $\tau = 1.52$ - Miranda

Figure 3.2: Plots of the tracked interfaces for the FronTier medium grid simulation VS the $f_1 = 0.5$ volume fraction isosurfaces for the Miranda simulation, at selected τ 's. Here, x -, y -, and z -directions are streamwise, spanwise, and vertical directions, respectively.

Miranda grid).

3.3 Molecular Mixing Parameter

In Fig. 3.4, we plot the molecular mixing parameter $\theta(\tau) = \langle f(1-f) \rangle / (\langle f \rangle \langle 1-f \rangle)$ on the center plane $z = 0$ of the mixing layer as a function of the dimensionless time τ for three FronTier simulations and one Miranda simulation, with the experimental data and its error bars superimposed. In this comparison, the nearly DNS (but not front tracked) Miranda simulation misses the experimental error bars for the final 2/3 of the experimental times, while the fine and medium FronTier simulations lie within these error bars, and the coarse FronTier grid barely misses them. See Fig. 3.4.

3.4 Velocity Variances

In the Miranda simulation [67], the average of a scalar field $\psi(\mathbf{x}, t)$ (denoted by a pair of angle brackets) is defined as the average over the xy -planes:

$$\langle \psi \rangle(z, t) = \frac{1}{L_x L_y} \int_0^{L_x} \int_0^{L_y} \psi(\mathbf{x}, t) dy dx. \quad (3.3)$$

According to $\psi(\mathbf{x}, t) = \langle \psi \rangle(z, t) + \psi'(\mathbf{x}, t)$, $\psi(\mathbf{x}, t)$ can be decomposed into mean and fluctuating (denoted by a prime) components. FronTier simulations yield lower values of center plane x and z directional velocity variances $\langle u'^2 \rangle$ and $\langle w'^2 \rangle$ than water-channel experimental data. Similar observations were reported by Mueschke et al., who ascribe the discrepancy between the Miranda simulation and the experimentally measured values of $\langle w'^2 \rangle$ beyond $\tau = 0.5$ to the limitation of grid resolution and computational

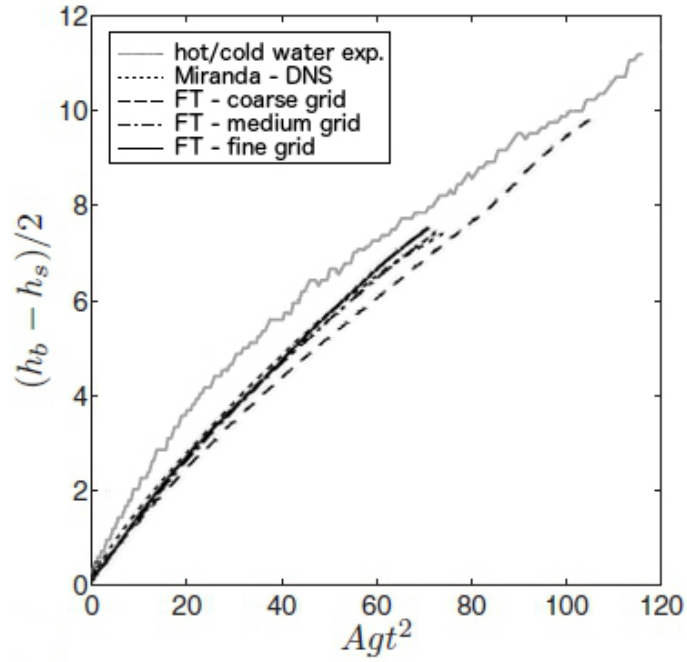


Figure 3.3: Plot of mixing zone growth for three FronTier simulations, one Miranda simulation and experimental data. The slower simulation growth at earlier times is likely due to incorrect modeling of the initial perturbations.

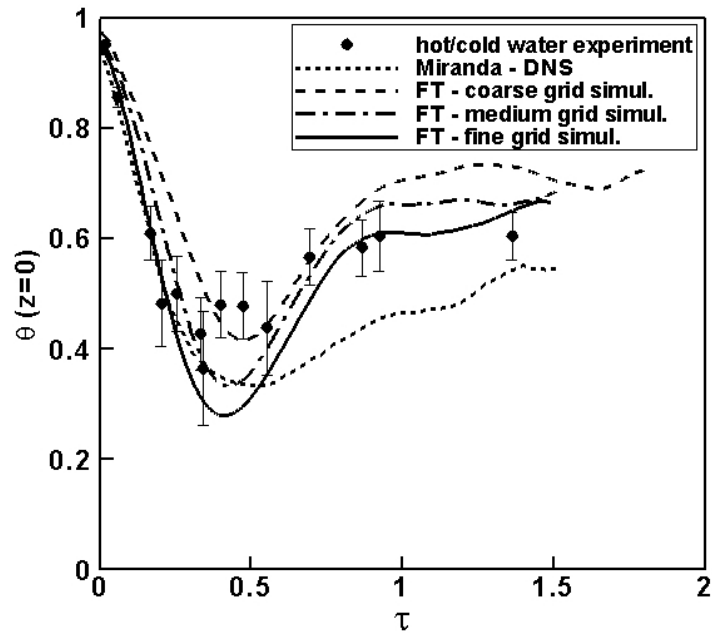


Figure 3.4: Plot of $\theta(\tau) = \langle f(1 - f) \rangle / (\langle f \rangle \langle 1 - f \rangle)$ on the center plane of the mixing zone as a function of the dimensionless time τ , for three FronTier simulations, one Miranda simulation and experimental data.

domain size. While the aliasing errors and loss of energy due to those limitations might affect the values of $\langle w'^2 \rangle$, we explain the simulation-experiment discrepancy of $\langle w'^2 \rangle$ from a differently point of view.

3.4.1 Particle-Image Velocimetry Diagnostics in Experiment

In water-channel experiment by Mueschke et al., velocity perturbations in the xz -plane were measured using a typical PIV diagnostics system [68], which consists of a digital imaging system, seeding particles, two alternating pulsed lasers with a series of cylindrical lenses, and a synchronizer to act as an external trigger for control of the digital imaging system and lasers, see Fig. 1.1 and 3.5. A series of 1200 images are recorded, which defines a type of time average. Velocity fields were determined by calculating the two-dimensional cross-correlation of two successive images using MATPIV v. 1.6.1. All outliers were removed by a local median filter and replaced by interpolated values. The MATPIV v. 1.6.1 post-processing algorithm employed a multi-pass technique, resulting in a final velocity field of 39×29 velocity vectors. 1199 velocity fields from 1200 images were combine into one analysis, in the sense that the u and w velocity components at a given point on the xz -plane were taken from each of the 1199 velocities to determine the velocity fluctuations.

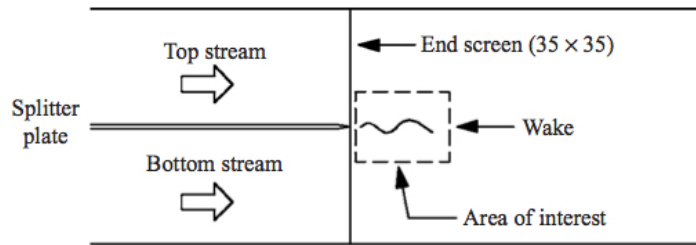


Figure 3.5: Schematic diagram of the region measured by the PIV diagnostics system in the water channel.

3.4.2 PIV Diagnostics VS FronTier Diagnostics

A careful examination of PIV and FronTier diagnostics provides insight into how to explain the discrepancy between the FronTier simulations and the experimentally measured values of $\langle w'^2 \rangle$. The PIV diagnostics and FronTier's differ mainly in two aspects:

1. The PIV diagnostics are in essence not be able to measure velocity vectors with a large spanwise velocity v (direction normal to the laser sheet), while FronTier simulations record all velocity vectors. The PIV diagnostics remove outliers and replace them by interpolated values. We could regard the velocity vectors that have too large a v -component velocity as outliers at least in FronTier diagnostics.

2. The PIV diagnostics average velocities over 39×29 interrogation windows, where the window size in the z -direction equals 1X grid size for FronTier medium grid and 2X for fine grid; the window size in the x -direction actually corresponds to some number of time steps.

In order to make FronTier diagnostics comparable to those from the PIV, modifications are made to FronTier diagnostics as follows. First, a velocity filter removes velocity vectors with a large spanwise velocity v . In the water-channel experiment, the laser sheet is parallel to xz -plane (streamwise-vertical) with a thickness of $L = 0.532 \mu\text{m}$. The water channel was seeded with Conduct-O-Fil silver-coated hollow glass spheres having a mean particle diameter $D_p = 13 \mu\text{m}$. The time interval between two successive laser pulses equals $\Delta T = 1/30 \text{ s}$. We model the escape velocity v_{esc} defined so that velocity vectors whose v -component exceeds v_{esc} will be discarded from FronTier diagnostics.

A basic model for estimating v_{esc} is proposed here. Suppose a particle is on the

laser sheet at the current laser pulse, i.e., $t = t_0$. The entering position of the particle is shown in Fig. 3.6. If this particle misses the second laser sheet at $t = t_0 + \Delta T$, then v should satisfy $|v| \cdot \Delta T > L + D_p$. Thus,

$$v_{esc} := \frac{L + D_p}{\Delta T} = 4.0596 \times 10^{-2} \text{ cm/s.} \quad (3.4)$$

For FronTier diagnostics, it is observed that the portion of outliers increases with time, see Table 3.1. This issue was not addressed in either the PIV analysis or the DNS diagnostics, which might introduce some discrepancy between the Miranda simulation analysis and the FronTier diagnostics. To further minimize any inconsistency between the PIV analysis and FronTier diagnostics, we reconstruct the missing data values for outliers. In FronTier diagnostics, the reconstructing technique employed by PIV analysis is applied to early times when the portion of outliers is reasonably small, and no significant effect was observed.

Second, the average of a field $\psi(\mathbf{x}, t)$ used by PIV diagnostics involves both space and time averaging. It can be expressed as

$$\langle \psi \rangle(z, t) = \frac{1}{2\Delta t} \frac{1}{L_x L_y} \int_{t-\Delta t}^{t+\Delta t} \int_0^{L_x} \int_0^{L_y} \psi(\mathbf{x}, \tau) dy dx d\tau. \quad (3.5)$$

Instead of using the space-averaged $\langle \psi \rangle$ defined in Eq. (3.3), FronTier diagnostics takes Eq. (3.5). FronTier uses 2X mesh average for the fine grid and 1X mesh average for the coarse and medium grids.

Good agreement for normalized vertical velocity variance $\langle w'^2 \rangle / AgH$ between experimental data and three FronTier simulations has been achieved, as shown in Fig. 3.7a. The velocity filter is important in achieving this agreement.

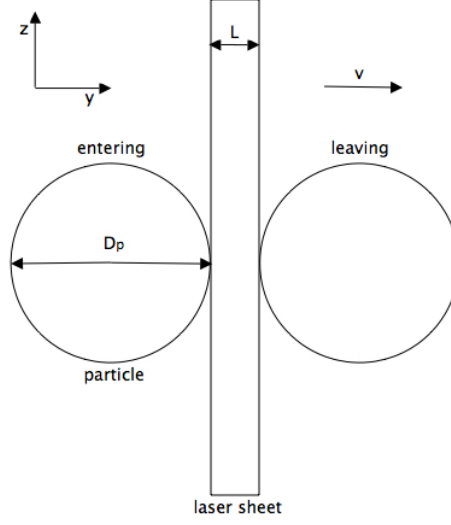
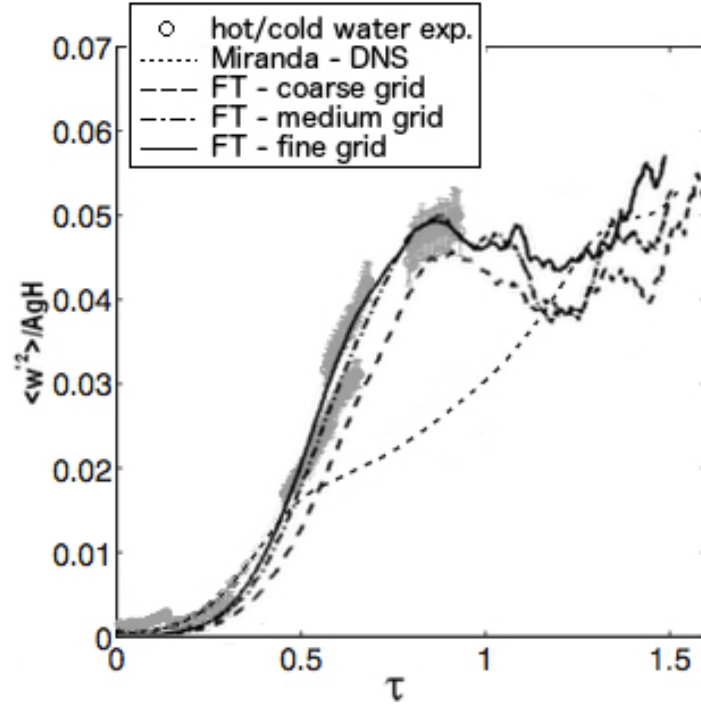


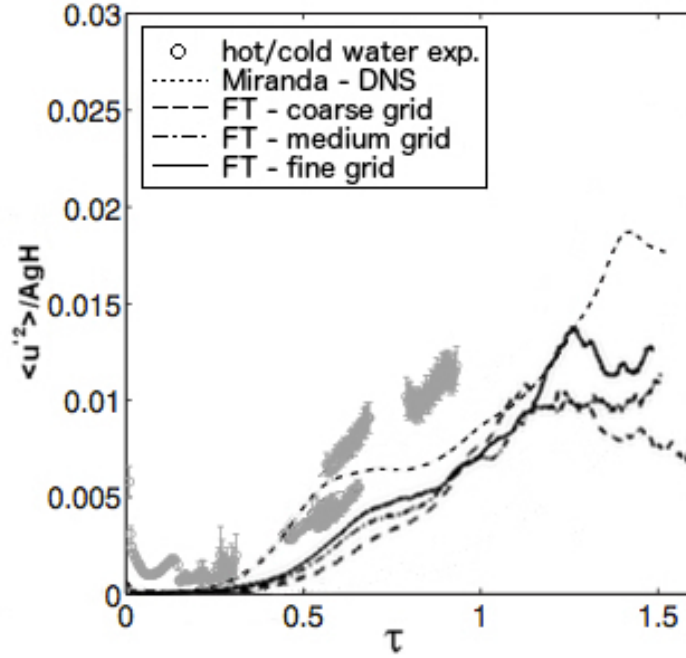
Figure 3.6: Schematic diagram of a basic model for estimating the escape velocity v_{esc} . It shows the entering and leaving positions of the particle with a mean particle diameter $D_p = 13 \mu\text{m}$. The laser sheet is parallel to the xz -plane, with a thickness of $L = 0.532 \mu\text{m}$.

Table 3.1: Table of selected percentage of outliers on FronTier fine grid

dimensionless time τ	percentage of outliers (%)
0.13	0
0.40	25.63
0.60	54.95
0.70	68.26
0.92	81.70
1.20	88.57
1.49	92.42

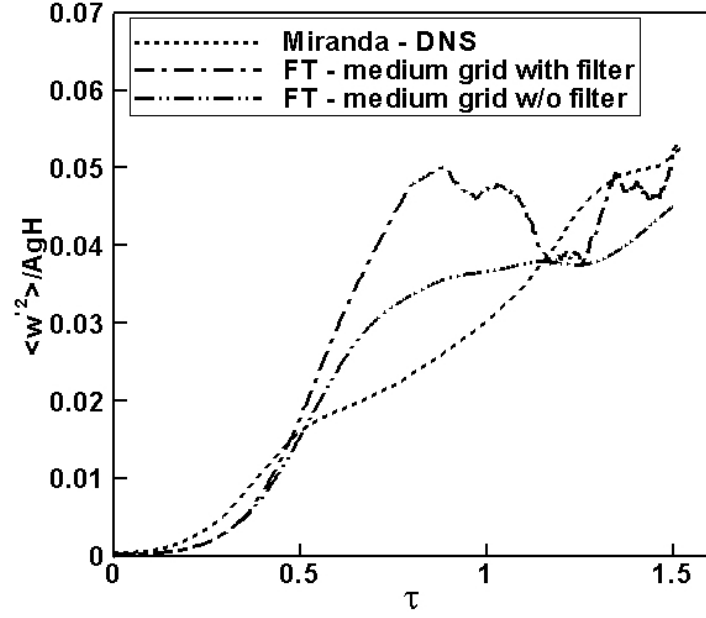


(a) normalized vertical velocity variance

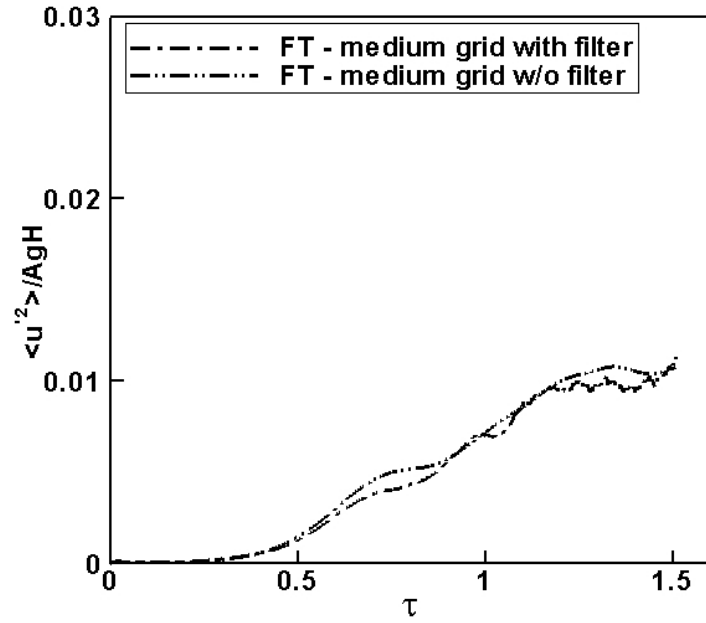


(b) normalized streamwise velocity variance

Figure 3.7: Plots of normalized vertical velocity variance $\langle w'^2 \rangle / AgH$ and streamwise velocity variance $\langle u'^2 \rangle / AgH$ for three FronTier simulations with the velocity filter and one Miranda simulation, with experimental data superimposed.



(a) normalized vertical velocity variance



(b) normalized streamwise velocity variance

Figure 3.8: Plots of normalized vertical velocity variance $\langle w'^2 \rangle / AgH$ and streamwise velocity variance $\langle u'^2 \rangle / AgH$ for FronTier simulation on the medium grid with and without the velocity filter.

3.5 Justification of the Omission of SGS Terms

Mixing can occur with or without turbulence. The present case is strongly mixing, but only transitionally or marginally turbulent. It is for this reason that front tracking but not SGS is important. SGS adds turbulent diffusion, not needed, while front tracking prevents unwanted numerical shear viscosity and diffusion. These numerical artifacts, in the absence of front tracking, introduce undesired and incorrect modifications to the fluid transport, even for shear viscosity, and even for a simulation resolved more finely than the Kolmogorov scale. From Fig. 3.4 we see the correctness of this choice, and also see the poorer agreement with experiment resulting from an ILES algorithm in which SGS terms are defined by numerical artifacts, even with a marginally turbulent flow with nearly DNS resolution. The low level of turbulence and the lack of need for SGS terms does not protect against artificial introduction of numerical artifacts.

We compute the dynamic SGS coefficients ν_{turb} and D_{turb} , as defined in [38, 63, 58]. Fig. 3.9 shows that the mean SGS coefficients in the RT unstable mixing zone are small relative to the molecular viscosity/diffusivity even for the FronTier coarse grid. Further, the plots of the mixing zone growth, molecular mixing parameter, and velocity variances with/without the SGS terms justify the omission of these terms, as seen in Fig. 3.10.

3.6 Discussion

A brief discussion of the statistical first/second moments in the FronTier simulations is as follow.

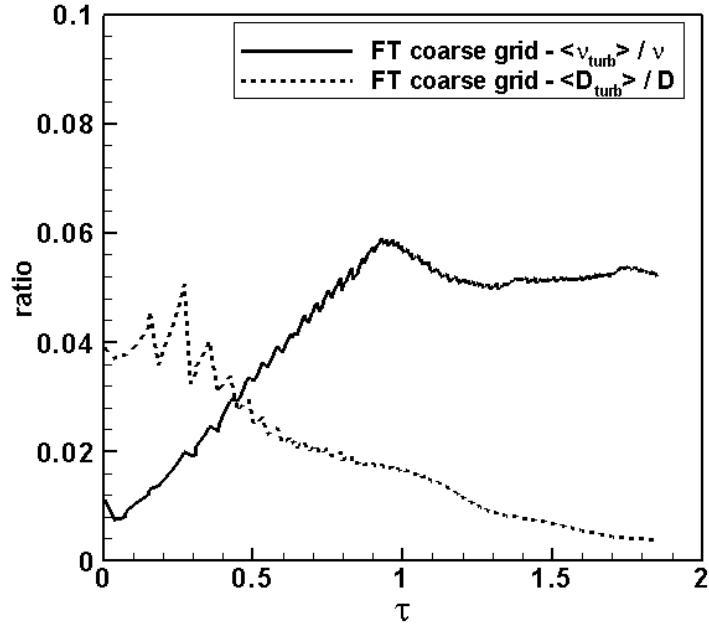


Figure 3.9: Plot of the ratios of the mean turbulent kinematic viscosity $\langle \nu_{\text{turb}} \rangle$ and diffusivity $\langle D_{\text{turb}} \rangle$ in the RT mixing zone to the molecular kinematic viscosity $\nu = (\mu_1 + \mu_2)/(\rho_1 + \rho_2)$ and diffusivity $D = \nu/\text{Sc}$. The SGS terms are small relative to the molecular viscosity/diffusion, even for the FronTier coarse grid.

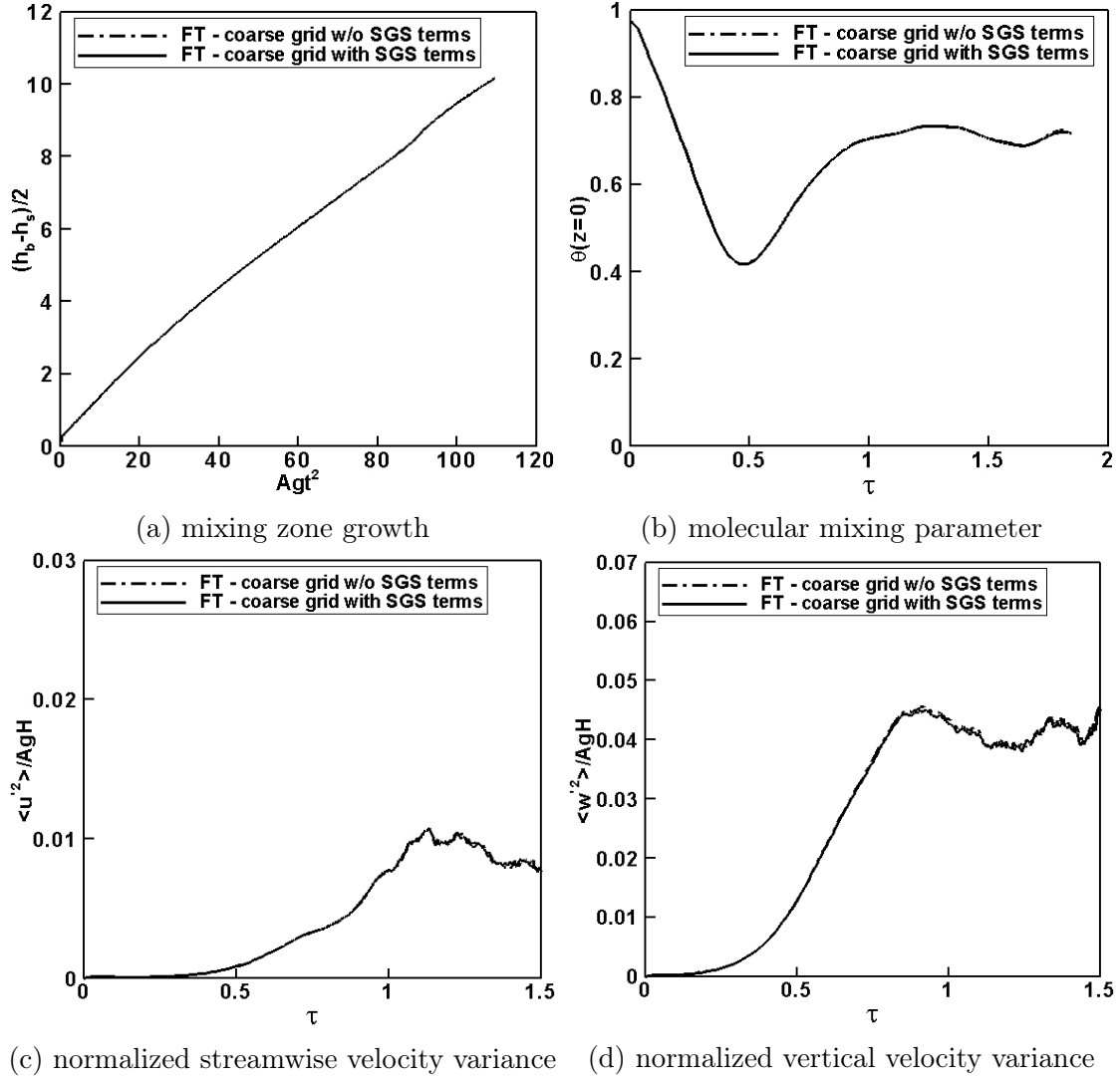


Figure 3.10: Plots of the mixing zone growth, molecular mixing parameter, and velocity variances for the FronTier coarse grid simulation with/without the SGS terms. In each plot, two curves are almost overlapped, even at late times.

1. The velocity variance of vertical velocity $\langle w'^2 \rangle$:

$\langle w'^2 \rangle$ is taken on the midplane of the mixing zone and shows stronger up/down drafts for the FronTier simulations and experiment, but weaker in the Miranda. The bubble/spike penetration distance or the growth rate α is about the same.

There might be compensating errors in Miranda: weaker up/down drafts in the bubbles and spikes on the midplane, probably smaller mushroom caps to reduce drag, and thus identical front motion.

FronTier simulations must enhance shear layers (as well as concentration gradients), so that there is less drag within the shear layer and it moves more freely with FronTier, and thus better following the experiment. This seems not to be an issue of the FronTier grid, as 8X, 4X, and 2X coarser grids in FronTier show the same results.

2. The molecular mixing parameter θ :

θ is a measure of the thermal mixing as observed on the midplane. FronTier shows more mixing, not less, compared to the Miranda. Again it is in good agreement with the experiment, in contrast to the Miranda.

The sign of the difference appears to be paradoxical, as FronTier has less thermal diffusion across a tracked front but we observe more in the data. Even the direction of the change needs an explanation.

A possible explanation is that the front interface, as it is traced out through the midplane is more complicated, and thus allows more thermal diffusion, even while eliminating the numerical thermal diffusion likely in the Miranda.

Note that this interface complexity is the reverse of the analysis of shear velocity, meaning that the FronTier advantage must overcome both Miranda's finer grid and

also Miranda's presumed simpler interface geometry in presenting less shear drag and larger up/down drafts in the bubbles/spikes. The verification of such statement needs to be provided in the future work.

Chapter 4

Conclusions

We have obtained good experimental validation for comparison to two of three statistical second moments measured in the hot-cold water splitter plate experiments [67]. Two aspects of this agreement are worth further comment.

First, we note the significant improvement relative to the results of the 10th-order compact stencil turbulence code Miranda, itself run at a nearly DNS level (grid resolution finer than the Kolmogorov scale and slightly above the Batchelor scale). There is no documentation we are aware of which sets the required resolution for convergence as a multiple of the Kolmogorov or Batchelor scales, but surely if ever established, it would depend on the solution functional for which convergence was desired and the level of convergence required. In any case our simulations are LES, and not nearly DNS, being two, four, and eight times coarser in resolution. Our simulations appear to show mesh convergence, an issue not studied with the single simulation reported in [67]. On the basis of these comments, we believe that the choice of algorithms is significant in simulations of statistical second moments, and that front tracking is an important aspect of a good algorithm to choose for turbulent mixing.

Secondly, details of data analysis matter. We attribute an initially observed simulation-experiment discrepancy to insufficient modeling of the data collection. Once this issue is accounted for, we find good levels of agreement for the vertical velocity second moment. We do not explain the only moderate success in our comparison to the second moment of the streamwise velocity.

To further improve the robustness of the current front tracking method, we plan to develop a selective tracking algorithm for the extremely complicated tangled regions. Also, the verification of our explanation to the FronTier results will be provided in the future work.

Bibliography

- [1] S. I. Abarzhi, J. Glimm, and K. Nishihara. Rayleigh-Taylor instability and Richtmyer-Meshkov instabilities for fluids with a finite density contrast. *Phys. Lett. A*, 11:1–7, 2003.
- [2] R. J. Adrian. Particle-imaging techniques for experimental fluid mechanics. *Annual Review of Fluid Mechanics*, 23:261–304, 1991.
- [3] R. J. Adrian. Twenty years of particle image velocimetry. *Experiments in Fluids*, 39:159–169, 2005.
- [4] A. S. Almgren, J. B. Bell, and W. G. Szymczak. A numerical method for the incompressible Navier-Stokes equations based on an approximate projection. *SIAM J. Sci. Comput.*, 17(2):358–369, 1996.
- [5] U. Alon, J. Hecht, D. Ofer, and D. Shvarts. Power laws and similarity of Rayleigh-Taylor and Richtmyer-Meshkov mixing fronts at all density ratios. *Phys. Rev. Lett.*, 74:534–538, 1995.
- [6] M. J. Andrews and S. B. Dalziel. Small Atwood number Rayleigh-Taylor experiments. *Phil. Trans. R. Soc. A*, 368:1663–1679, 2010.
- [7] S. W. Armfield, N. Williamson, M. P. Kirkpatrick, and R. Street. A divergence

- free fractional-step method for the Navier-Stokes equations on non-staggered grids. *Anziam J.*, 51:654–667, 2010.
- [8] Satish Balay, Kris Buschelman, Victor Eijkhout, William D. Gropp, Dinesh Kaushik, Matthew G. Knepley, Lois Curfman McInnes, Barry F. Smith, and Hong Zhang. PETSc users manual. Technical Report ANL-95/11 - Revision 3.5, Argonne National Laboratory, 2014.
 - [9] J. B. Bell, P. Colella, and H. M. Glaz. A second order projection method for the incompressible Navier-Stokes equations. *J. Comput. Phys.*, 85:257, 1989.
 - [10] J. B. Bell, P. Colella, and L. H. Howell. An efficient sceond-order projection method for viscous incompressible flow. In *Proceedings of the Tenth AIAA Computational Fluid Dynamics Conference*, page 360. AIAA, 1991.
 - [11] D. J. Benson. An efficient, accurate, simple ALE method for nonlinear finite element programs. *Computer Methods in Applied Mechanics and Engineering*, 72:305–350, 1989.
 - [12] D. J. Benson. Computational methods in Lagrangian and Eulerian hydrocodes. *Computer Methods in Applied Mechanics and Engineering*, 99:235–394, 1992.
 - [13] D. J. Benson. Momentum advection on a staggered mesh. *J. Comput. Phys.*, 100:143–162, 1992.
 - [14] W. Bo, X. Liu, J. Glimm, and X. Li. A robust front tracking method: Verification and application to simulation of the primary breakup of a liquid jet. *SIAM J. Sci. Comput.*, 33:1505–1524, 2011.
 - [15] W. L. Briggs, V. E. Henson, and S. F. McCormick. *A Multigrid Tutorial (2nd ed.)*.

Society for Industrial and Applied Mathematics, Philadelphia, PA, 2000. ISBN 0-89871-462-1.

- [16] D. Brown, R. Cortez, and M. Minion. Accurate projection method for the incompressible Navier Stokes equations. *J. Comput. Phys.*, 168:464–499, 2001.
- [17] K. D. Burrows, V. S. Smeeton, and D. L. Youngs. Experimental investigation of turbulent mixing by Rayleigh-Taylor instability, II. AWE Report Number 0 22/84, 1984.
- [18] B. M. Cetegen and K. D. Kasper. Experiments on the oscillatory behaviour of buoyant plumes of helium and helium-air mixtures. *Phys. Fluids*, 8:2974–2984, 1996.
- [19] S. Chandrasekhar. The character of equilibrium of an incompressible heavy viscous fluid of variable density. *Proc. Camb. Phil. Soc.*, 51:162–178, 1955.
- [20] S. Chandrasekhar. *Hydrodynamic and Hydromagnetic Stability*. Oxford University Press, Oxford, 1961.
- [21] A. J. Chorin. Numerical solution of the Navier Stokes equations. *Math. Comp*, 22:745–762, 1968.
- [22] A. J. Chorin. On the convergence of discrete approximations to the Navier-Stokes equations. *Math. Comp*, 23:341, 1969.
- [23] B. Clark, N. Ray, and X. Jiao. Surface mesh optimization, adaption and untangling with high-order accuracy. *21st International Meshing Roundtable*, 2012.
- [24] A. W. Cook and P. E. Dimotakis. Transitional stages of Rayleigh-Taylor instability. *J. Fluid Mech.*, 443:69, 2001.

- [25] S. B. Dalziel, P. F. Linden, and D. L. Youngs. Self-similarity and internal structure of turbulence induced by Rayleigh-Taylor instability. *J. Fluid Mech.*, 399:1–48, 1999.
- [26] J. Donea, S. Giuliani, and J. P. Halleux. An arbitrary Lagrangian-Eulerian finite element method for transient dynamic fluid-structure interactions. *Computer Methods in Applied Mechanics and Engineering*, 33:689–723, 1982.
- [27] P. G. Drazin and W. H. Reid. *Hydrodynamic Stability, 2nd ed.* Cambridge University Press, New York, 2004.
- [28] D. Drikakis and W. Rider. *High-Resolution Methods for Incompressible and Low-Speed Flows*. Springer, 2005.
- [29] Jian Du, Brian Fix, James Glimm, Xicheng Jia, Xiaolin Li, Yunhua Li, and Lingling Wu. A simple package for front tracking. *J. Comput. Phys.*, 213:613–628, 2006.
- [30] R. E. Duff, F. H. Harlow, and C. W. Hirt. Effects of diffusion on interface instability between gases. *Phys. of Fluids*, 5:417–425, 1962.
- [31] H. W. Emmons, C. T. Chang, and B. C. Watson. Taylor instability of finite surface waves. *J. Fluid Mech.*, 7:177–193, 1960.
- [32] E. Fermi. Taylor instability of an incompressible fluid. In E. Segre, editor, *Collected Papers of E. Fermi*. University Of Chicago Press, Chicago, 1965.
- [33] J. R. Freeman, M. J. Clauser, and S. L. Thompson. Rayleigh-Taylor instabilities in inertial-confinement fusion targets. *Nucl. Fusion*, 17:223–230, 1977.

- [34] B. Fryxell, K. Olson, P. Ricker, F. X. Timmes, M. Zingale, D. Q. Lamb, P. MacNeice, R. Rosner, J. W. Truran, and H. Tufo. FLASH: An adaptive mesh hydrodynamics code for modeling astrophysical thermonuclear flashes. *Astrophysical Journal ,Supplement*, 131:273, 2000.
- [35] V. N. Gamezo, A. M. Khokhlov, E. S. Oran, A. Y. Chtchelkanova, and R. O. Rosenberg. Thermonuclear supernovae: Simulations of the deflagration stage and their implications. *Science*, 299:77–81, 2003.
- [36] E. George, J. Glimm, X.-L. Li, Y.-H. Li, and X.-F. Liu. The influence of scale-breaking phenomena on turbulent mixing rates. *Phys. Rev. E*, 73:016304, 2006.
- [37] E. George, J. Glimm, X.-L. Li, A. Marchese, and Z.-L. Xu. A comparison of experimental, theoretical, and numerical simulation Rayleigh-Taylor mixing rates. *Proc. National Academy of Sci.*, 99:2587–2592, 2002.
- [38] M. Germano, U. Piomelli, P. Moin, and W. H. Cabot. A dynamic subgrid scale eddy viscosity model. *Phys. Fluids A*, 3:1760–1765, 1991.
- [39] J. Glimm, J. W. Grove, X.-L. Li, K.-M. Shyue, Q. Zhang, and Y. Zeng. Three dimensional front tracking. *SIAM J. Sci. Comput.*, 19:703–727, 1998.
- [40] J. Glimm, H. Lim, R. Kaufman, and W. Hu. Euler equation existence, nonuniqueness and mesh converged statistics. *Phil. Trans. R. Soc. A*, 2014. Stony Brook University Preprint SUNYSB-AMS-14-04.
- [41] J. Glimm, B. Plohr, and D. Sharp. Large eddy simulation, turbulent transport and the renormalization group. 2013. Los Alamos National Laboratory Preprint Number LA-UR-12-26149, Stony Brook University Preprint Number SUNYSB-AMS-12-02.

- [42] J. Glimm and D. H. Sharp. Chaotic mixing as a renormalization group fixed point. *Phys. Rev. Lett.*, 64:2137–2139, 1990.
- [43] J. Glimm, D. H. Sharp, T. Kaman, and H. Lim. New directions for Rayleigh-Taylor mixing. *Phil. Trans. R. Soc. A*, 371:20120183, 2013. Los Alamos National Laboratory Preprint LA-UR 11-00423 and Stony Brook University Preprint SUNYSB-AMS-11-01.
- [44] V. N. Goncharov. Analytical model of nonlinear, single-mode, classical Rayleigh-Taylor instability at arbitrary atwood numbers. *Phys. Rev. Lett.*, 88:134502–134506, 2002.
- [45] P. N. Guzdar, P. Satyanarayana, J. D. Huba, and S. L. Ossakow. Influence of velocity shear on Rayleigh-Taylor instability. *Geophys. Res. Letts.*, 9:547, 1982.
- [46] F. Harlow and J. Welch. Numerical study of large-amplitude free-surface motion. *Phys. Fluids*, 9:842, 1966.
- [47] J. Hilditch and P. Colella. A projection method for low Mach number fast chemical reaction flow, 1997. URL http://crd.lbl.gov/assets/pubs_presos/AMCS/ANAG/A227.pdf.
- [48] C. Hirt and B. Nichols. Volume of fluid (VOF) method for the dynamics of free boundaries. *J. Comput. Phys.*, 39:201–225, 1981.
- [49] C. W. Hirt, A. A. Amsden, and J. L. Cook. An arbitrary Lagrangian-Eulerian computing method for all flow speeds. *J. Comput. Phys.*, 14:227–253, 1974. Reprinted in **135** (1997), pp. 203–216.
- [50] X. Jiao and H. Zha. Consistent computation of first- and second-order differential

- quantities for surface meshes. In *Proceedings of the ACM Solid and Physical Modeling Symposium*, pages 159–170, 2008.
- [51] D. D. Joseph. Fluid dynamics of two miscible liquids with diffusion and gradient stress. *Eur. J. Mech., B/Fluids*, 9:565–596, 1990.
 - [52] T. Kaman, R. Kaufman, J. Glimm, and D. H. Sharp. Uncertainty quantification for turbulent mixing flows: Rayleigh-Taylor instability. In A. Dienstfrey and R. Boisvert, editors, *Uncertainty Quantification in Scientific Computing*, volume 377 of *IFIP Advances in Information and Communication Technology*, pages 212–225. Springer, 2012. Stony Brook University Preprint number SUNYSB-AMS-11-08.
 - [53] R. Kaufman, H. Lim, and J. Glimm. Conservative front tracking: the algorithm, the rationale and the API. *Bulletin of the Institute of Mathematics, Academia Sinica New Series*, submitted, 2015. Stony Brook University Preprint SUNYSB-AMS-15-01.
 - [54] A. M. Khokhlov. Propagation of turbulent flames in supernovae. *ApJ*, 449:695–713, 1995.
 - [55] D. Layzer. On the instability of superimposed fluids in a gravitational field. *Astrophys. J.*, 122:1–12, 1955.
 - [56] H. Lim, J. Iwerks, J. Glimm, and D. H. Sharp. Nonideal Rayleigh-Taylor mixing. *Proc. Nat. Acad. Sci.*, 107(29):12786–12792, 2010. Stony Brook University Preprint SUNYSB-AMS-09-05 and Los Alamos National Laboratory Preprint LA-UR 09-06333.
 - [57] H. Lim, J. Iwerks, Y. Yu, J. Glimm, and D. H. Sharp. Verification and validation of

- a method for the simulation of turbulent mixing. *Physica Scripta*, T142:014014, 2010. Stony Brook University Preprint SUNYSB-AMS-09-07 and Los Alamos National Laboratory Preprint LA-UR 09-07240.
- [58] H. Lim, Y. Yu, J. Glimm, X. L. Li, and D. H. Sharp. Subgrid models for mass and thermal diffusion in turbulent mixing. *Physica Scripta*, T142:014062, 2010. Stony Brook Preprint SUNYSB-AMS-08-07 and Los Alamos National Laboratory Preprint LA-UR 08-07725.
- [59] Hyunkyung Lim, Yijie Zhou, Valmor F. de Almeida, and James Glimm. Fully developed turbulent mixing in an annular sector. In *Hyperbolic Problems: Theory, Numerics, Applications*, page 623, Springfield, MO, 2012. American Institute of Mathematical Sciences. AIMS on Applied Mathematics, Volume 8.
- [60] John D. Lindl. *Inertial Confinement Fusion*. Springer-Verlag, New York, 1998.
- [61] X.-F. Liu, E. George, W. Bo, and J. Glimm. Turbulent mixing with physical mass diffusion. *Phys. Rev. E*, 73:056301, 2006.
- [62] Lord Rayleigh. Investigation of the character of the equilibrium of an incompressible heavy fluid of variable density. In *Scientific Papers*, volume II, page 200. Cambridge Univ. Press, Cambridge, England, 1900.
- [63] T. Ma. *Large eddy simulation of variable density flows*. PhD thesis, University of Maryland, 2006.
- [64] L. G. Margolin. Introduction to “an arbitrary Lagrangian-Eulerian computing method for all flow speeds”. *J. Comput. Phys.*, 135:198–202, 1997.
- [65] M. Minion. On the stability of Godunov-projection methods for incompressible flow. *J. Comput. Phys.*, 123:435–449, 1996.

- [66] R. Mittal and G. Iaccarino. Immersed boundary methods. *Annu. Rev. Fluid Mech.*, 37:239–261, 2005.
- [67] N. Mueschke and O. Schilling. Investigation of Rayleigh-Taylor turbulence and mixing using direct numerical simulation with experimentally measured initial conditions. I. Comparison to experimental data. *Physics of Fluids*, 21:014106 1–19, 2009.
- [68] Nicholas Mueschke, Malcolm Andrews, and Oleg Schilling. Experimental characterization of initial conditions and spatio-temporal evolution of a small Atwood number Rayleigh-Taylor mixing layer. *J. Fluid Mech.*, 567:27–63, 2006.
- [69] S. Osher and J. Sethian. Fronts propagating with curvature-dependent speed: Algorithms based on Hamilton-Jacobi equations. *Jour. Comp. Phys*, 79:12–49, 1988.
- [70] J. M. Ottino. Mixing and chemical reactions: A tutorial. *Chemical Engineering Science*, 49:4005–4027, 1994.
- [71] C. S. Peskin. Numerical analysis of blood-flow in heart. *J. Comput. Phys.*, 25(3):220–252, 1977.
- [72] R. D. Petraso. Rayleigh’s challenge endures. *Nature*, 367:217–218, 1994.
- [73] E. G. Puckett, A. S. Almgren, J. B. Bell, D. L. Marcus, and W. J. Rider. A high-order projection method for tracking fluid interfaces in variable density incompressible flows. *J. Comput. Phys.*, 130:269–282, 1997.
- [74] P. Ramaprabhu and M. Andrews. Experimental investigation of Rayleigh-Taylor mixing at small atwood numbers. *J. Fluid Mech.*, 502:233–271, 2004.

- [75] P. Ramaprabhu and G. Dimonte. Single-mode dynamics of the Rayleigh-Taylor instability at any density ratio. *Phys. Rev. E*, 71:036314–036323, 2005.
- [76] N. Ray, D. Wang, X. Jiao, and J. Glimm. High-order numerical integration over discrete surfaces. *SIAM Journal Numerical Analysis*, 50:3061–3083, 2012.
- [77] K. I. Read. Experimental investigation of turbulent mixing by Rayleigh-Taylor instability. *Physica D*, 12:45–58, 1984.
- [78] Y. Saad and M.H. Schultz. GMRES: A generalized minimal residual algorithm for solving nonsymmetric linear systems. *SIAM J. Sci. Stat. Comput.*, 7:856–869, 1986.
- [79] D. H. Sharp. An overview of Rayleigh-Taylor instability. *Physica D*, 12:3–18, 1984.
- [80] V. S. Smeeton and D. L. Youngs. Experimental investigation of turbulent mixing by Rayleigh-Taylor instability (part 3). AWE Report Number 0 35/87, 1987.
- [81] D. M. Snider and M. J. Andrews. Rayleigh-Taylor and shear driven mixing with an unstable thermal stratification. *Phys. Fluids*, 6(10):3324–3334, 1994.
- [82] E. Y. Tau. A second-order projection method for the incompressible Navier-Stokes equations in arbitrary domains. *J. Comput. Phys.*, 115:147–152, 1994.
- [83] G. I. Taylor. The instability of liquid surfaces when accelerated in a direction perpendicular to their planes I. *Proc. R Soc. London A*, 201:192–196, 1950.
- [84] S. R. Tieszen. On the fluid mechanics of fires. *Annu. Rev. Fluid Mech.*, 33:67–92, 2001.
- [85] G. Tryggvason, B. Bunner, A. Esmaeeli, D. Juric, N. Al-Rawahi, W. Tauber,

- J. Han, S. Nas, and Y.-J. Jan. A front-tracking method for the computations of multiphase flow. *J. Comput. Phys.*, 169:708–759, 2001.
- [86] W. S. D. Wilcock and J. A. Whitehead. The Rayleigh-Taylor instability of an embedded layer of low viscosity fluid. *J. Geophys. Res.*, 96:12193, 1991.
- [87] D. L. Youngs. Numerical simulation of turbulent mixing by Rayleigh-Taylor instability. *Physica D*, 12:32–44, 1984.
- [88] Q. Zhang. Analytical solution of the Layzer-type approach to unstable interface fluid mixing. *Phys. Rev. Lett.*, 81(16):3391–3394, 1998.
- [89] Y. Zhou. *Front Tracking Method with High-Order Enhancement and Its Application in Two-Phase Micromixing of Incompressible Viscous Fluids*. PhD thesis, State University of New York at Stony Brook, 2014.
- [90] Y. Zhou, N. Ray, H. Lim, S. Wang, V. F. de Almeida, J. Glimm, X.-L. Li, and X. Jiao. Development of a front tracking method for two-phase micromixing of incompressible viscous fluids with interfacial tension in solvent extraction. Technical Report ORNL/TM-2012/28, Oak Ridge National Laboratory, 2012.
- [91] M. Zingale, S. E. Woosley, C. A. Rendleman, M. S. Day, and J. B. Bell. Three-dimensional numerical simulations of Rayleigh-Taylor unstable flames in type Ia supernovae. *ApJ.*, 632:1021–1034, 2005.